POLITECNICO DI MILANO

Dipartimento di Chimica, Materiali e Ingegneria Chimica

Master of Science in Materials Engineering

Survey on Strain Hardening of Wiredrawn Stainless Steel

Advisor   :   Prof. Carlo MAPELLI

Master thesis by :   Enver Tugrul OZBECENE

Coskun UNLER

Academic Year 2011 – 2012

POLITECNICO DI MILANO

Dipartimento di Chimica, Materiali e Ingegneria Chimica

Master of Science in Materials Engineering

Survey on Strain Hardening of Wiredrawn Stainless Steel

Thesis by   :   _____
                            (Enver Tugrul OZBECENE)

                _____
                            (Coskun UNLER)

Advisor   :   _____
                            (Prof. Carlo MAPELLI)

Academic Year 2011 – 2012

Contents

List of Figures

List of Tables

Abstract

The purpose of this study is to understand the effects of deformation in terms of area reduction, to strain hardening behavior of AISI 316L austenitic stainless steels and AISI 430 ferritic stainless steels which are deformed by the wire drawing process.

Chapter 1 is the introduction part explains briefly the procedure and the methodology performed in this study. Chapter 2 covers the general review of the literature about deformation, strain hardening phenomenon, wire drawing process and tensile testing. Chapter 3 also covers the general review of the literature about microstructural characterization and EBSD analysis. In Chapter 4, experimental methodology of microstructural characterization, tensile testing and EBSD analysis, and mechanical information of the materials are mentioned. Chapter 5 shows the results and their discussions, all the experimental results of the tests and analyses were published. Finally, with the help of the data obtained from all the tests and analyses, the correlation between strain hardening behavior and wire drawing process is discussed.

Keywords: *wire drawing; AISI 316L austenitic stainless steel; AISI 430 ferritic stainless steel; strain hardening; plastic deformation; tensile testing; EBSD analysis; texture*

1 Introduction

Stainless steels are one of the most widely used engineering materials in the industry. Stainless steel wires are mostly used in construction and related industry. They are also used for redrawing, mesh weaving, soft pipe, steel rope, filter elements, making of spring, etc.

The most used technique for the production of stainless steel wires in the wire manufacturing industry is the wire drawing process that can be defined as a metalworking process in which the cross-section of an initial wire is reduced by pulling the wire through a series of drawing dies. This process is one of the oldest metal forming techniques that are used in steel industry [1].

During any cold metal forming process, such as wire drawing, the metal is plastically deformed and gets harder and stronger through plastic deformation. This phenomenon is called strain hardening [2].

The purpose of this study is to understand the effect of deformation in terms of area reduction, to strain hardening behavior of AISI 316L austenitic stainless steels and AISI 430 ferritic stainless steels which are deformed by the wire drawing process. In order to understand this relationship between wire drawing process and the strain hardening phenomenon, samples of as produced base materials with the diameter of 9 mm for both type of stainless steels and samples of wire drawn stainless steels with the diameters of 8 mm, 7 mm and 6.5 mm for both type, are examined.

Examination of the microstructural characteristics of all the samples is done with the reflective optical microscopy. Then wire drawing is simulated with tensile testing in terms of the amount of deformation applied during the process and the strain hardening exponents of all the samples are obtained. After the examination of the trend of the strain hardening exponents, EBSD technique is used to acquire information about the textures formed during both wire drawing and tensile testing.

Finally, thanks to the data obtained from all the tests and analyses, the correlation between strain hardening behavior and wire drawing process is discussed.

2   Deformation and Strain Hardening

In materials science, a variation of a body shape or size due to an applied force in which the deformation energy is transferred through work, or a change in temperature where the deformation energy is transferred through heat, is called deformation. The possible forces for the first case can be tensile, compressive, shear, torsion or bending. In the second case, the most significant factor, which is determined by the temperature, is the mobility of the structural defects such as point vacancies, dislocations, grain boundaries, stacking faults and twins in both crystalline and non-crystalline solids. The movement or displacement of such mobile defects is thermally activated, and thus limited by the rate of atomic diffusion. Deformation is usually described as strain (ε) [3] [4].

2.1   Stress-Strain Relationship

The level in which a material deforms itself depends on the magnitude of an applied stress. Stress and strain are proportional to each other for most metals that are stressed in tension only at relatively low levels, according to the relationship reported in Equation 2.1.1 which is known as Hooke's Law, where σ (MPa) is the applied stress, ε (mm/mm) is the strain and E (GPa) is the modulus of elasticity and often called as Young's modulus [5].

$$\sigma = E\varepsilon$$
<div align="right">**Equation 2.1.1**</div>

Deformation can be classified as elastic deformation and plastic deformation according to the permanence of the change in the shape. Hooke's Law is only valid for the elastic region. For the plastic region, the relationship between the stress and strain is not linearly proportional.

2.1.1   Elastic Deformation

When stress and strain are proportional in a deformation state, it is called elastic deformation. In Figure 2.1.1 a linear relationship of stress versus strain is shown. The slope of this linear region is the elasticity modulus (E). This modulus can be considered as a material's resistance to elastic deformation. In an elastic region of a material, when the applied load is released, the material returns to its original shape which means that elastic deformation is not permanent. Application of the load corresponds to moving from the origin up and along the straight line.

By the release of the load, the line is reversed in the opposite direction, back to the origin as shown in Figure 2.1.1 [5].
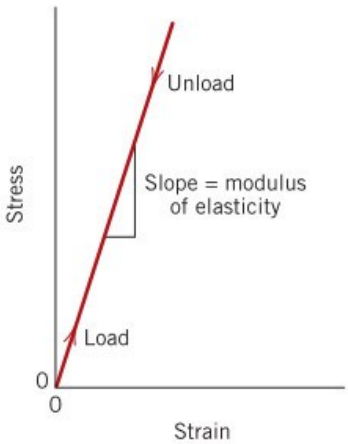
Figure 2.1.1 Schematic stress-strain diagram of linear elastic deformation region [5]

2.1.2 Plastic Deformation

Elastic deformation persists only to strains of about 0.005 for most metallic materials. As more deformation is applied, the stress is no longer proportional to strain (Hooke's law in Equation 2.1.1 is no longer valid), and permanent and non-recoverable plastic deformation occurs. The tensile stress–strain behavior into the plastic region for a typical metal is plotted schematically in Figure 2.1.2. For most metals, the transition from elastic to plastic occurs gradually [5].
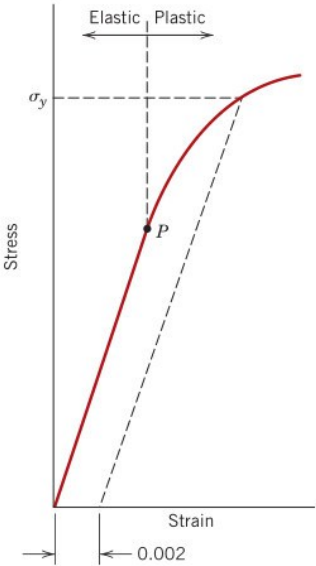
Figure 2.1.2 Schematic stress-strain diagram of plastic deformation region [5]

4

From atomistic approach, plastic deformation means that large number of atoms break their bonds with the original neighbors and then rebuild new bonds with their new neighbors as they move relative to one another; due to the movement of dislocations there, upon removal of the stress they do not return to their original positions which results in a permanent shape change of the material [5].

2.2 Strain Hardening

Under slow loading and unloading a ductile metal (such as steel) will behave according to the stress-strain diagram as in Figure 2.2.1(a). Between the points O and A which corresponds to the elastic region of the material, loading and unloading result simply going up and down. On the other hand, if loading is performed up to the point B which lies in the plastic deformation region, the path of B-e-C (approximately parallel to O-A) is followed during the unloading which results in a permanent deformation with the amount of O-C. Upon reloading from point C, again an elastic behavior with the path of C-f-D is observed which is slightly different from the unloading path and point D becomes the new yield point for the partially deformed condition of the material. A comparison of points A and D shows that plastic deformation has made the material stronger. If the test were again interrupted at point E, a new and even higher-yield stress would be revealed. The phenomenon described above is known as strain hardening which means that metals get harder and stronger, when they are plastically deformed. If a stress is capable of producing plastic deformation, an even greater stress will be required to continue the flow [6].

Strain hardening (also called work-hardening) is the process of making a metal harder and stronger through plastic deformation. When a metal is plastically cold deformed, dislocations move and additional dislocations are generated. The more dislocations within a material, the more they will interact and become pinned or tangled. This will result in a decrease in the mobility of the dislocations and a strengthening of the material. This type of strengthening is commonly called cold-working because the plastic deformation must occurs at a temperature low enough that atoms cannot rearrange themselves. When a metal is worked at higher temperatures (hot-working) the dislocations can rearrange and little strengthening is achieved [2].

2.2.1 Strain Hardening Exponent

Different metals are strain-hardened at different rates; therefore, different metals will show different increases in strength for the same amount of plastic deformation. One method of describing this behavior is to mathematically fit the plastic deformation region of the stress-strain diagram to a power form as reported in Equation 2.2.1 which is the true stress-strain relationship of the material and assign the best-fit value of the strain hardening exponent (n), which is the slope of the plastic portion of the true stress-true strain curve. [6] [7].

$$\sigma = K\,\varepsilon^n$$

Equation 2.2.1

A metal with a high value of strain hardening exponent will have a high increase in strength with a small amount of plastic deformation where a metal with a small strain hardening exponent will show a little increase in strength with deformation. This behavior can be seen in Figure 2.2.1(b) [8].
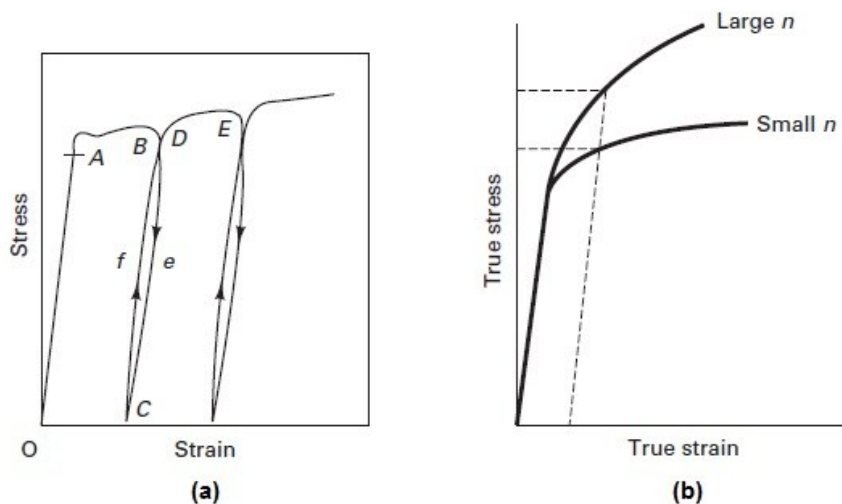
Figure 2.2.1 (a) Stress-strain diagram obtained by loading and unloading a specimen. (b) True stress-true strain curves for metals with large and small strain hardening [6]

2.3 Wire Drawing

Drawing is a metalworking process achieved by pulling a metal piece through a die by applying a tensile force to the exit side of the die. The process can be named as bar, rod or wire drawing according to the diameter of the final product. As shown in Figure 2.3.1 cross-sectional area is reduced by passing the material through the die. The main variables in the drawing process can be listed as: reduction of the cross-sectional area, number of the

sequence used for the total drawing process, speed of drawing, friction in the die-metal interface and angle of the die [5] [9] [10].
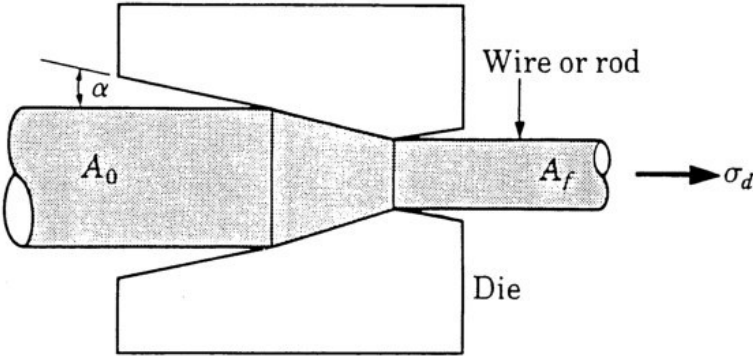
Figure 2.3.1 Schematic of wire drawing process [11, pp. 72-83]

Wire drawing usually starts with a coil of hot-rolled rod. After cleaning the surface of the rod by pickling to remove any grading on the surface which could result surface defects or die wear, the rod is lubricated to decrease the friction along the die-metal interface. The rod can be passed through the die after surface cleaning and lubrication [9].

Indirect compression causes deformation of the workpiece during drawing. That is, the stress applied to the exiting product (σ_d in Figure 2.3.1) causes compression against the die face and deforms the material. The maximum drawing force that can be applied is limited by the yield strength of the exiting product to avoid deformation or fracture after the wire has come out from the die. Wire drawing is can either be done by bench drawing as seen in Figure 2.3.2 and block drawing as seen in Figure 2.3.3 [8] [9].

Block drawing is usually used rather than the draw bench when the rod diameter is small enough to allow coiling, because coiling allows the production of long lengths in a much smaller space as seen in Figure 2.3.2 and Figure 2.3.3 [9].
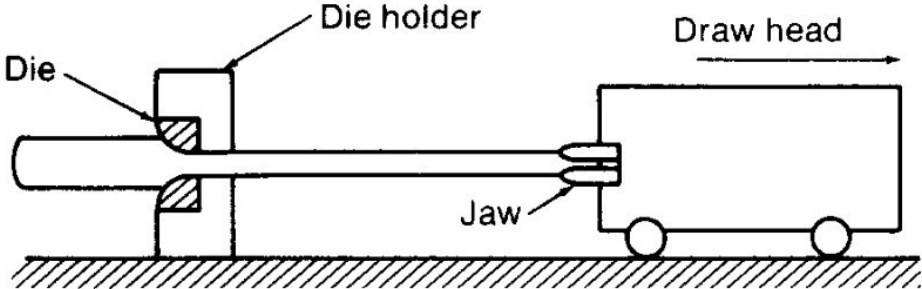
Figure 2.3.2 Schematic drawing of a draw bench [9]

7
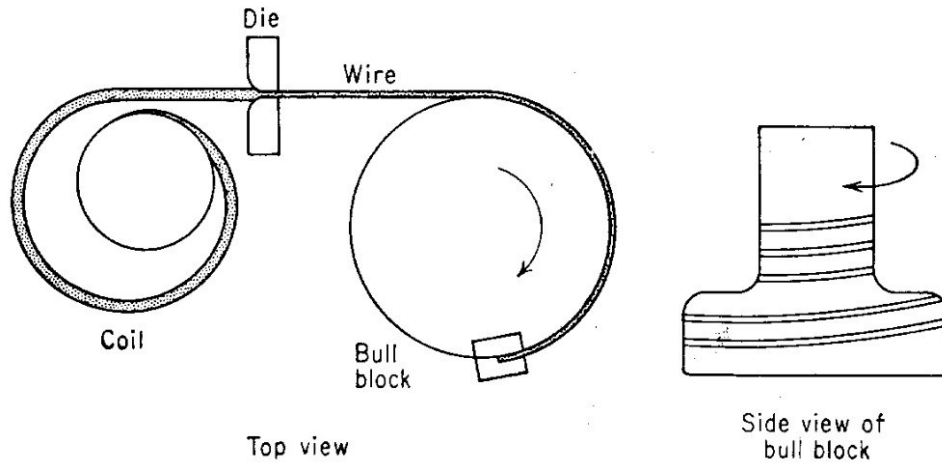
Figure 2.3.3 Schematic drawing of a block drawing [9]

This study focuses only on the reduction of the cross-sectional area among other variables of the wire drawing process because the aim of the study is to relate the strain hardening behavior of the material to the amount of reduction of the cross-sectional area. Samples used in the study are readily wiredrawn and all the other parameters of the process are related to the quality of the process and the quality of the output products.

2.4 Tensile Testing

Tensile test is the standard way to characterize an engineering material mechanically. Indeed, from tensile test, it is possible to define all the parameters useful for static design of component, such as yield strength, ultimate tensile strength and fracture strength. Moreover, with the same experimental setup usually used to perform tensile test, it is possible to study the effect of controlled and user-defined plastic deformation applied on a material, in order to investigate mechanical and physical properties.

For the tensile test, as seen in Figure 2.4.1, a given length of wire (L_0) of cross-sectional area (A_0) is elongated progressively usually at a constant rate. Variables in tensile test can be listed as: pulling force (F), and measure of elongation (L-L_0), (L_0 is the initial length and L is the increased length at an instant of the test). Figure 2.4.2 is a representation of a formal specimen design for rods with a reduced section where d_0 is the original diameter of the parallel length of a circular test piece, L_c is the parallel length of the reduced section of the test specimen, L_0 original gauge length, L_t is the total length of the test piece and S_0 the original cross-sectional area of the parallel length. In the tensile testing of wire, it is usually impractical to use a

reduced section, and the gage length is simply placed between the points of gripping [10] [12].
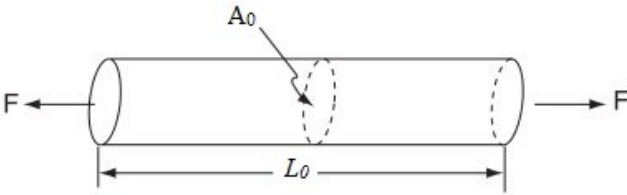
Figure 2.4.1 A schematic representation of the starting configuration of a round tensile specimen [10]
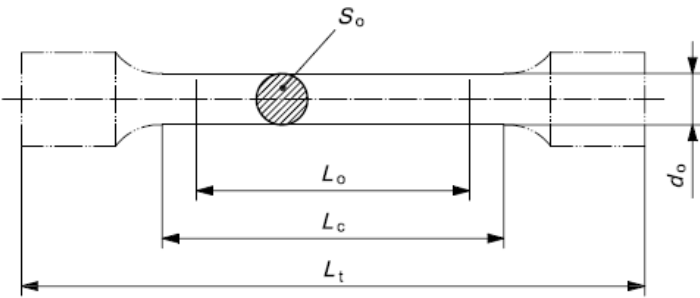
Figure 2.4.2 A formal tensile test specimen with a reduced section [12]

A tensile test can be performed on a dedicated machine such as shown in Figure 2.4.3, where the one end of the specimen is gripped by a moving crosshead, while the other hand is fixed to a non-moving platen. The force applied is then measured by a load cell placed in series with the sample, while the elongation and the elongation rate are measured by an extensometer which is attached directly on the specimen where the gage length is marked [10].
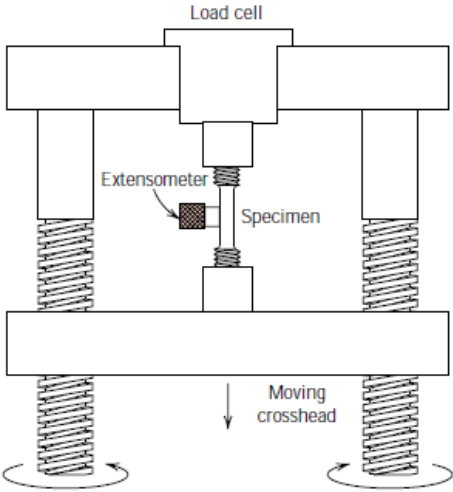
Figure 2.4.3 Schematic representation of the machine used to perform tensile tests [5]

2.4.1 Engineering and True Stress-Strain Diagram

There are two common approaches to define stress and strain; one of them is engineering stress-strain and the other one is true stress-strain. Proper system should be used for the most appropriate technical situation [10].

The output of a tensile test is usually recorded on a computer as force versus elongation. Specimen size affects these force-elongation characteristics, therefore the effect of geometry is eliminated simply by dividing the force to the initial cross-sectional area to calculate the engineering stress, σ_e, as in Equation 2.4.1 and dividing the elongation to the initial gauge length to calculate engineering strain, ε_e, as in Equation 2.4.2. These engineering stress and strain values are calculated by assuming the cross-sectional area is constant during the entire testing [5] [10].

$$\sigma_e = \frac{F}{A_0}$$

Equation 2.4.1

$$\varepsilon_e = \frac{(L - L_0)}{L_0}$$

Equation 2.4.2

By using the corresponding stress and strain data, a diagram like in Figure 2.4.4(a) can be drawn. Point A in both Figure 2.4.4(a) and Figure 2.4.4(b) represents the starting condition of the test. The region between the points A and B is called the elastic region. Point B is the beginning of the plastic deformation and is called the Yield Strength of the material which is the stress required to produce a very slight yet specified amount of plastic strain (usually 0.02% deformation). The point C corresponds to the Ultimate Tensile Strength which is the maximum stress that a material can resist while being pulled before necking [9] [10].
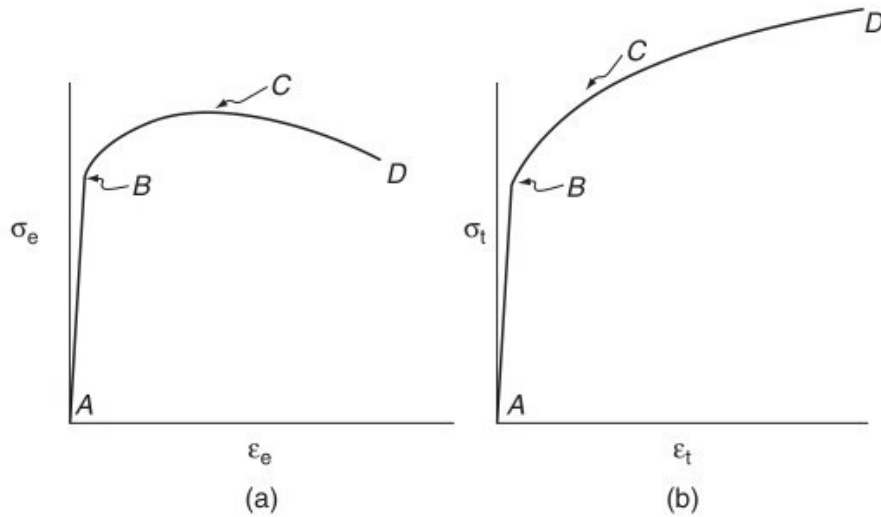
Figure 2.4.4 (a) Schematic of engineering stress-strain diagram (b) Schematic of true stress-strain diagram [10]

In Figure 2.4.4(a), when we go beyond the point C, the material seems to become weaker. In fact, the actual case is the material continues strengthening. Due to the localizing of the stresses in the necking region, the cross-sectional area decreases rapidly which results in the load-bearing capacity of the sample. The stress, calculated from Equation 2.4.1, is based on the initial cross-sectional area, and does not take into account this reduction of the necking area [5] [9].

Some situations require using true stress and strain values. As in the Equation 2.4.3, the force divided by the cross-sectional area at any instance of the test (A), is defined as true stress (σ_T) [5].

$$\sigma_T = \frac{F}{A}$$ **Equation 2.4.3**

In addition, strain can be represented in a more convenient way that is the true strain (ε_T), as in the Equation 2.4.4 [5].

$$\varepsilon_T = ln\frac{L}{L_0}$$ **Equation 2.4.4**

3 Microscopic Examination

On occasion it is necessary or desirable to examine the structural elements and defects that influence the properties of materials. For example, the shapes and average size or diameters of the grains for a polycrystalline sample are important structural characteristics. In most materials the constituent grains are of microscopic dimensions, having diameters that may be on the order of microns, and their details must be investigated using some type of microscope. Optical, electron, and scanning probe microscopes are commonly used in microscopy. These instruments aid in investigations of the microstructural features of all material types [5].

In this study, optical microscopy technique is used for the microstructural characterization to examine the change in the grain size and to observe how the grains are elongated and aligned by the applied plastic deformation. And also, Electron Backscattered Diffraction (EBSD) method is used for the detailed texture analysis which is the analysis of the alignment of crystallographic planes to the sample reference system and fibers present in the microstructure of the materials.

3.1 Microstructural Characterization

In this work, reflective optical microscopy is used to investigate the microstructure; optical and illumination systems are its basic elements. The light microscope must be used in a reflecting mode for materials that are opaque to visible light (all metals, many ceramics and polymers), and only the surface is observed. Differences in reflectivity of the various regions of the microstructure result in contrasts in the image produced [5].

Normally, to reveal the important details of the microstructure, careful surface preparations are necessarily should be done. The specimen surface must first be ground and polished to a smooth and mirror-like finish. This is accomplished by using successively finer abrasive papers and powders. The microstructure is revealed by a surface treatment by an etching in an appropriate chemical reagent. The chemical reactivity of the grains of some single-phase materials depends on crystallographic orientation. Consequently, etching characteristics vary from grain to grain in a polycrystalline specimen. Figure 3.1.1(b) shows how normally incident light is reflected by three etched surface grains, each having a different orientation.

Figure 3.1.2(a) depicts the surface structure as it might appear when viewed with the microscope; the luster or texture of each grain depends on its reflectance properties [5].
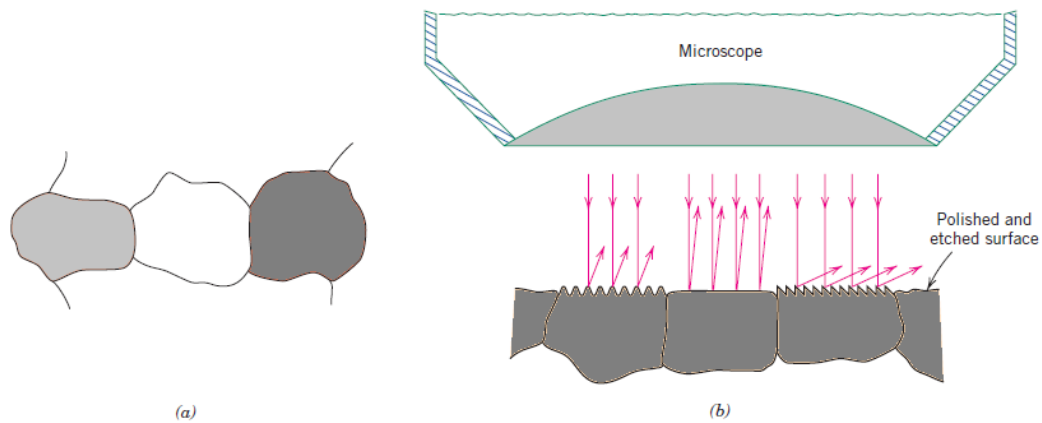
Figure 3.1.1 (a) Polished and etched grains as they might appear when viewed with an optical microscope. (b) Section taken through these grains showing how the etching characteristics and resulting surface texture vary from grain to grain because of differences in crystallographic orientation [5].

Also, small grooves form along grain boundaries as a consequence of etching. Since atoms along grain boundary regions are more chemically active, they dissolve at a greater rate than those within the grains. These grooves become discernible when viewed under a microscope because they reflect light at an angle different from that of the grains themselves; this effect is displayed in Figure 3.1.2(a). Figure 3.1.2(b) is a micrograph of a polycrystalline specimen in which the grain boundary grooves are clearly visible as dark lines [5].
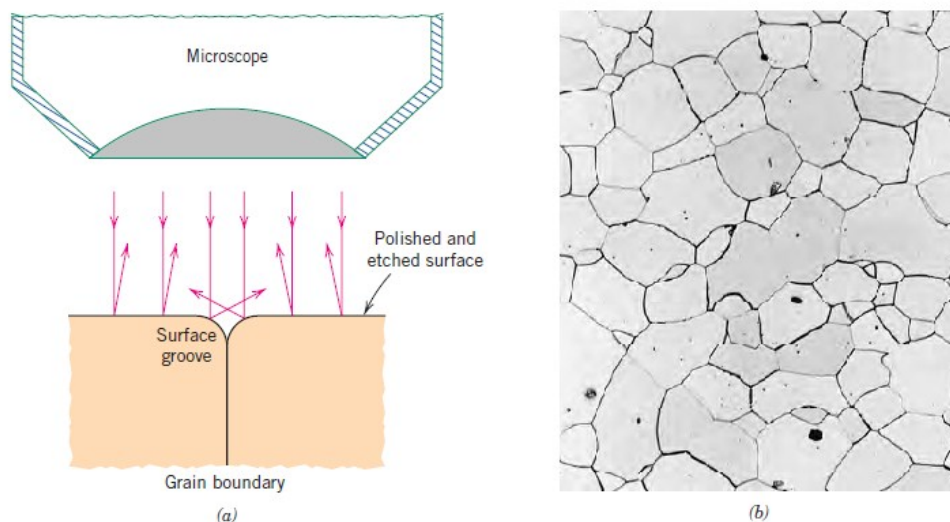
Figure 3.1.2 (a) Section of a grain boundary and its surface groove produced by etching; the light reflection characteristics in the vicinity of the groove are also shown. (b) Micrograph of the surface of a polished and etched polycrystalline specimen of an iron-chromium alloy in which the grain boundaries appear dark (100x) [5].

When the microstructure of a two-phase alloy is to be examined, an etchant is often chosen that produces a different texture for each phase so that the different phases may be distinguished from each other [5].

3.2 EBSD

The term "electron backscatter diffraction" (EBSD) is referred with both the scanning electron microscope (SEM) technique and the kind of probe that can be attached to the microscope. Quantitative microstructural information about the crystallographic nature of metals, semiconductors, minerals and ceramics, in fact most inorganic crystalline materials can be provided from EBSD. It reveals grain size, grain boundary character, grain orientation, texture, and phase identity of the sample under the beam. Centimeter-sized samples with millimeter-sized grains, to metal thin films with nano-grains may be analyzed. The macroscopic sample size is dependent on the ability of the SEM's stage and chamber to orient a sample at 70° tilt at an appropriate working distance, usually in the range 5 to 30 mm [13].

EBSD operates by arranging a flat, highly polished (or as-deposited thin film) sample at a shallow angle, usually 20°, to the incident electron beam (Fig. 2.7) (since the SEM stage is often used to tilt the plane of the sample to this shallow angle, the value of stage tilt is often referred to and is typically 70°). With an accelerating voltage of 10–30 kV, and incident beam currents of 1–50 nA, electron diffraction occurs from the incident beam point on the sample surface. With the beam stationary, an EBSD pattern emanates spherically from this point. There are several discussions of the electron interactions involved; in particular Wells [14], gives a good descriptions of the competing theories [13].

3.2.1 Data Analysis with EBSD

Investigation and analysis of the acquired data set is often performed away from the SEM with related data processing software that allows a great variety of analyses to be performed: grain size analysis, textural (preferred crystallographic orientation) analysis, and many modes of microstructural visualization and analysis with orientation maps. In this study polar and inverse polar figures, orientation distribution functions (ODF) and the coincidence site lattice (CSL) and misorientation data will be analyzed in order to observe the preferred crystallographic orientations in the microstructure [13].

3.2.1.1 Description of Textures

The common metals of industrial practice are polycrystalline aggregates in which each of the individual grains has an orientation that differs from those of its neighbors. It is quite unusual for the grains in such metals to have a random distribution of orientations, and the non-random distributions that occur are called preferred orientations or textures. These purely crystallographic characteristics should not be confused with alignment of the grain structure, or the preferred distributions of second phases in an alloy which are revealed by optical metallography. Equiaxed grain structures frequently exhibit texture and it is possible, at least in principle, for an elongated grain structure to be randomly oriented. Textures are developed at all stages of the manufacturing process of the metals but the precise nature of the texture is a complex function of the mechanical and thermal treatments as well as the material itself [15].

Deformation textures have their origins in the crystallographic nature of the common deformation processes of slip and twinning. Where large strains are involved, slip is usually the major factor but twinning can also be highly significant in texture development because of the massive re-orientations that are involved. During the slip process the crystal lattice rotates as a result of the shape change and the geometrical constraints of its surroundings. The restricted number of slip systems available produces rotations towards a limited number of end-points and so a deformation texture is produced. It is clear that the resulting texture will depend on the nature of the imposed stress (or strain) system, the extent of deformation, and the operative deformation modes which are themselves defined by the crystal structure and atomic bonding [15].

3.2.1.2 Pole Figures

Preferred orientations are usually described by means of pole figures. These are simple stereographic projections which show the distribution of particular crystallographic directions in the assembly of grains that constitute the metal. If the pole figure is to have any meaning, it must also contain some reference directions and these are usually chosen so that they correspond to easily defined directions in the specimen. In rolled sheet (drawn wire in this study), for example, it is natural to think in terms of the rolling direction (*RD*), the transverse direction (*TD*), and the sheet normal plane (*ND*). Figure 3.2.1(a) shows how the sheet is considered to sit at the center of the stereographic sphere with the orthogonal reference directions as x, y and z axes. The orientation of a single grain in the sample can be

represented by plotting its three (100) poles at the appropriate angular positions relative to the reference directions. The result is a pole figure, in this case a (100) pole figure, showing the positions of the (100) poles for the grain and, therefore, the orientation of the grain in the sheet as shown in Figure 3.2.1(b). For a polycrystalline sample all the grains must be considered and three (100) poles must be plotted for each to give the pole figure. In real metals the poles tend to cluster together in certain areas of the pole figure to produce a texture as shown schematically in Figure 3.2.1(c). The number of grains is normally such that the determination of individual orientations is impractical and the plotting of individual poles impossible. To overcome these difficulties it is usual to collect data from many grains simultaneously and to present this in the form of density contours on the pole figure. Figure 3.2.1(d) and (e) show how the pole density may be visualized and presented as contour lines on the stereographic projection [16] [15].
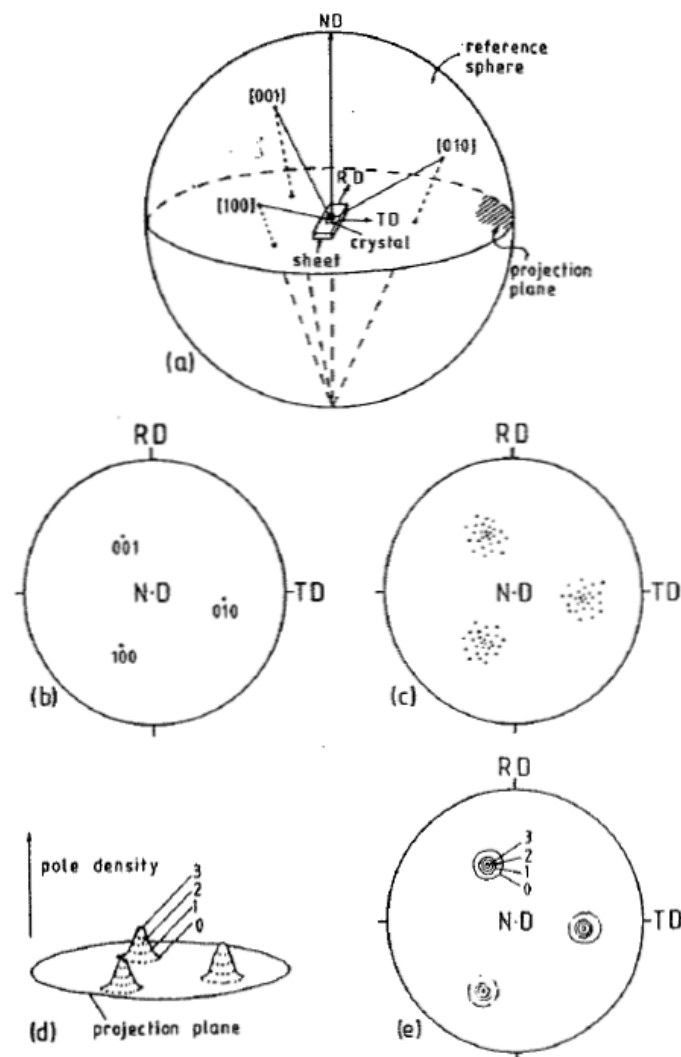
Figure 3.2.1 (a) Projection sphere and reference directions, (b) Projection of poles for a single grain, (c) Projection of poles from textured grains, (d) Pole density distribution, (e) Contour map of pole density [15]

3.2.1.3 Inverse Pole Figures

Rather than representing the orientation of the crystal coordinate system in the specimen coordinate system, that is, in a pole figure, vice versa the orientation of the specimen coordinate system can be projected into the crystal coordinate system. This representation is called the inverse pole figure. Thus, the reference system of the inverse pole figure is the crystal coordinate system, and the "orientation" is defined by the axes of the specimen coordinate system, for example, RD, TD, and ND [17].

As it is indicated by its name, the inverse pole figure is a sort of 'opposite' to the pole figure. While the pole figure shows how the specified crystallographic direction of grains are distributed in the sample reference frame, the inverse pole figure shows how the selected direction in the sample reference frame is distributed in the reference frame of the crystal. For example, normal direction inverse pole figure, lets us know which crystallographic directions in the polycrystalline material are most likely parallel to the sample normal direction. Since the properties of many important engineering materials are strongly direction-dependent, the inverse pole figure is very useful in predicting and calculating the average properties of polycrystalline material along a chosen direction.

Due to the crystal symmetry, a complete inverse pole figure usually contains many areas where the same information is repeated. For example, there are 24 symmetric sections in a inverse pole figure for cubic system, as shown in Figure 3.2.2(a). Practically, only one section is used as shown in Figure 3.2.2(b) [18].

(a) (b)
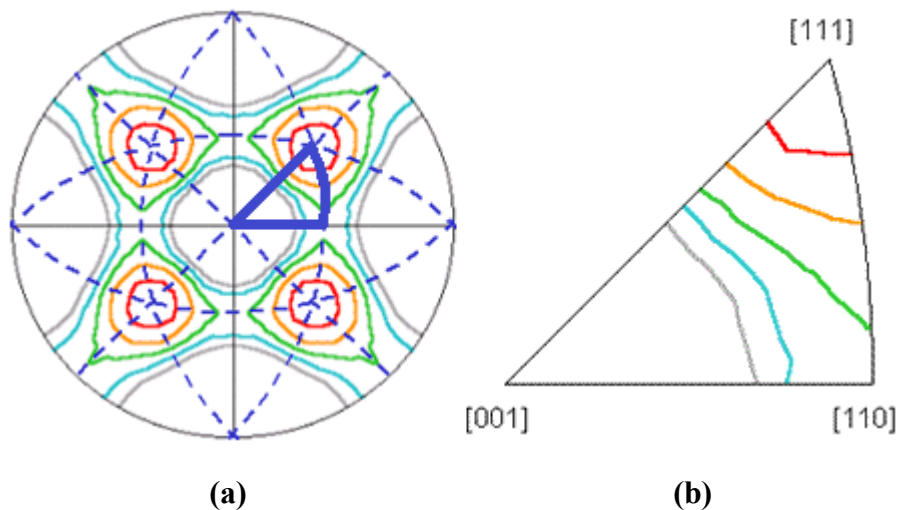
Figure 3.2.2 (a) A complete inverse pole figure (b) A partial inverse pole figure [18]

Inverse pole figure (IPF) orientation component uses a basic RGB coloring scheme, fit to an inverse pole figure. For cubic phases, full red, green, and blue are assigned to grains whose <100>, <110> or <111> axes, respectively, are parallel to the projection direction of the IPF (typically, the surface-normal direction). Intermediate orientations are colored by an RGB mixture of the primary components. Although the IPF orientation map is not susceptible to "wraparound" color speckling as in the total Euler scheme, it has its own limitations. Most notable is the coloring of pixels only by the projection-parallel crystallographic axis, independent of rotation about that axis. Thus grains with identical axes parallel to a specified IPF projection direction will have the same color in the IPF-based scheme, but may be in significantly different orientations. For example, two grains with <100> parallel to the surface normal are both colored red, but possess 30° of relative rotation about that axis. IPF-based orientation maps are most useful for displaying materials with strong fiber-textures and for understanding preferred orientations parallel to a sample direction of interest [17].

3.2.1.4 Orientation Distribution Functions

The information provided by the pole figures is a statistical distribution of a single direction and this information is not enough to obtain the complete orientation of individual grains or volume elements. The orientation of all the discrete volumes in the aggregate is described better by the ODF which was developed originally for materials with cubic crystallography and orthorhombic sample symmetry [19].

The orientation of a particular element which has the orientation (hkl)[uvw], can be described in terms of three Euler angles (Φ, φ_1 and φ_2). The crystallographic axes are represented in the normal way in a standard projection and the specimen orientation is specified by the reference directions ND and RD as shown in Figure 3.2.3(a). The angles Φ and φ_2 completely specify the direction ND. RD lies in the plane normal to ND and the angle φ_1 completely specifies the direction RD. Because three variables have been used to define (hkl)[uvw], the ODF can only be displayed as a three dimensional plot with the three Euler angles as axes as shown in Figure 3.2.3(b). [19].
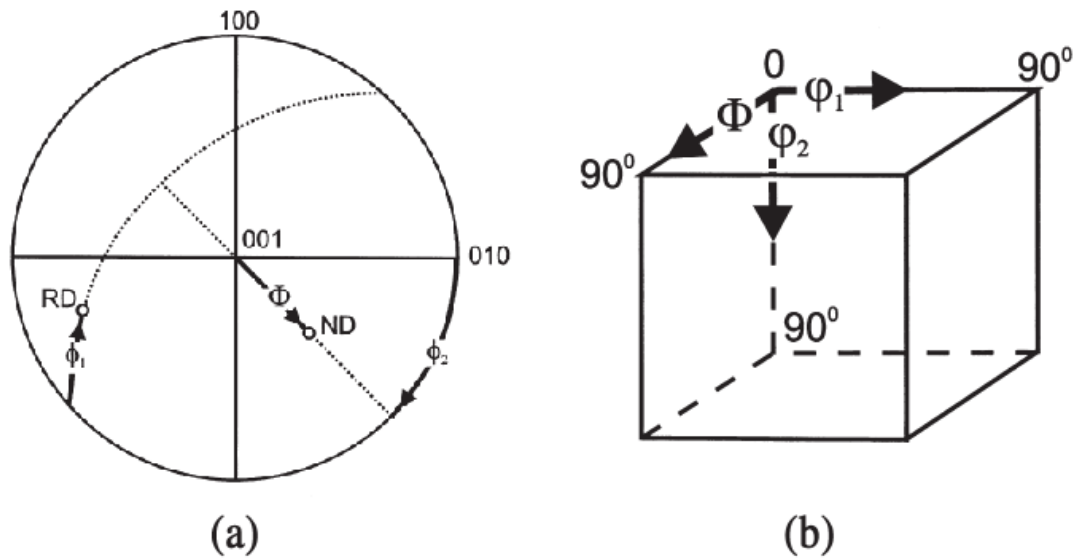
Figure 3.2.3 (a) Definition of Euler angles (b) Location of Euler angles in ODF space [19]

The ODF allows the identification of texture fibers as shown in Figure 3.2.4 and quantitative plots of intensity along these fibers provide very detailed information. Some important orientations and their Euler angles obtained from these quantitative plots of ODF's can be listed as in Table 3.2.1 [19]
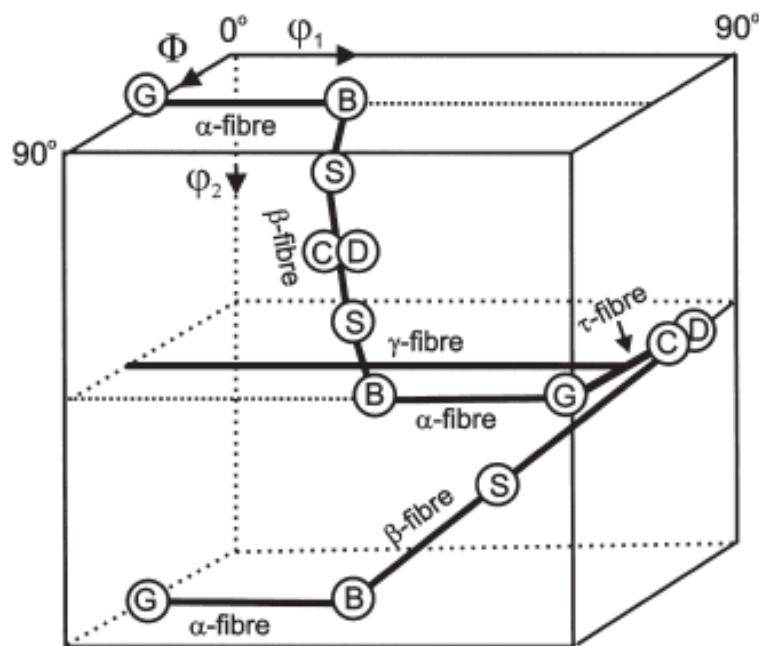
Figure 3.2.4 Plot of important fibres in ODF space [19]

Component, symbol	{hkl}	<uvw>	φ_1	Φ	φ_2
Copper, C	112	111	90	35	45
S	123	634	59	37	63
Goss, G	011	100	0	45	90
Brass, B	011	211	35	45	90
Dillamore, D	4,4,11	11,11,8	90	27	45
Cube	001	100	0	0	0

Table 3.2.1 Some important texture components in cubic metals [19]

4 Experimental Procedure

4.1 Introduction

In this study, austenitic stainless steel of grade AISI 316L and ferritic stainless steel of grade AISI 430 are examined under optical microscope for microstructural characteristics. Also mechanical properties are examined by tensile testing and after tensile testing, texture analyses are obtained under SEM by EBSD probe. All the procedures are explained in detail in the following subchapters.

4.2 Materials

4.2.1 General Information about the Materials

4.2.1.1 AISI 316L Austenitic Stainless Steel

AISI 316 is an austenitic chromium-nickel stainless steel containing molybdenum. This addition increases general corrosion resistance, improves resistance to pitting from chloride ion solutions, and provides increased strength at elevated temperatures. Corrosion resistance is improved, particularly against sulfuric, hydrochloric, acetic, formic and tartaric acids, acid sulfates and alkaline chlorides. AISI 316L is an extra-low carbon version of AISI 316 that minimizes harmful carbide precipitation due to welding. Typical uses include exhaust manifolds, furnace parts, heat exchangers, jet engine parts, pharmaceutical and photographic equipment, valve and pump trim, chemical equipment, digesters, tanks, evaporators, pulp, paper and textile processing equipment, parts exposed to marine atmospheres and tubing. AISI 316L is used extensively for weldments where its immunity to carbide precipitation due to welding assures optimum corrosion resistance. The chemical compositions of AISI 316 and AISI 316L austenitic stainless steels are given in Table 4.2.1 [20] [21].

Grade	Composition, wt %							
	C	Mn	Si	Cr	Ni	P	S	Other
316	0.08	2.00	1.00	16.0-18.0	10.0-14.0	0.045	0.03	2.0-3.0 Mo
316L	0.03	2.00	1.00	16.0-18.0	10.0-14.0	0.045	0.03	2.0-3.0 Mo

Table 4.2.1 Chemical composition of standard AISI 316 and 316L austenitic stainless steels [21]

4.2.1.2 AISI 430 Ferritic Stainless Steel

AISI 430 ferritic stainless steel is one of the most widely used of the straight chromium, ferritic stainless steels. It combines good corrosion resistance and heat and oxidation resistance up to 816°C with good mechanical properties. Typical consumer product applications include automotive trim and molding, furnace combustion chambers, dishwashers, range hoods, gas burners on heating units, gutters and downspouts, steam iron bases and flatware. Industrial and commercial applications range from interior architectural applications to nitric acid plant equipment, oil refinery equipment, roofing and siding and restaurant equipment. The chemical composition of AISI 430 ferritic stainless steel is given in Table 4.2.2 [21] [22].

Grade	Composition, wt %							
	C	Mn	Si	Cr	Ni	P	S	Other
430	0.12	1.00	1.00	16.0-18.0	---	0.04	0.03	---

Table 4.2.2 Chemical composition of standard AISI 430 ferritic stainless steel [21]

4.2.2 Samples Used in This Study

In this study there are four round wire (rod) samples with different diameters for both AISI 316L and AISI 430 stainless steels. The diameters of the samples are 9, 8, 7 and 6.5 mm. The 9 mm sample is the base material for the wire drawing process which is provided from ACERINOX, S.A., a Spanish steelmaking plant, while other samples are provided from Eure Inox s.r.l., an Italian steel shaping company, and produced sequentially by wire drawing process starting from 9 mm base material. Each wire product with smaller diameter is produced from the former wire product with one step larger diameter. The samples will be referred in the following chapters by their diameter.

4.3 Microstructural Characterization

From the provided wire products of both grades of steel, small representative pieces both cross-sectional and longitudinal-sectional are cut with abrasive disc cutter and molded into bakelite in order to handle easily.

After molding, eight samples (four cross-sectional and four longitudinal) of both AISI 316L and AISI 430 stainless steels are grinded starting from 320 grit SiC abrasive paper followed

by 600, 800, 1200 and 2500 grit SiC papers, respectively. Then, all the samples are polished on the velvet with 6, 3 and 1 μm diamond paste suspension, respectively. Before every polishing step, an ultrasound cleaning was done for about 1-2 min. to avoid any residual particle from the previous step of polishing which can cause scratching of the surface.

The next step after polishing is etching of the samples. Different methods of etching are applied with different etchants for each grade of steels. For the AISI 316L stainless steel samples electro-etching is done in 10% oxalic acid solution for approximately 20-40 seconds at 5 V and 10 A. However, for the AISI 430 stainless steel the etchant used is glyceregia solution (3 parts of glycerol, 3 parts of HCl, 1 part of HNO_3). The samples dipped into the solution for about 50-60 seconds as in regular etching process. The proper etchants are selected according to the reference [23].

Etched samples are then observed under the optical microscope, Leitz ARISTOMET, and optical micrographs are obtained. The results of the microstructural characterization will be discussed in Chapter 5.1.

4.4 Tensile Testing

4.4.1 Specimen Preparation

Specimens for the tensile testing are prepared according to ISO 6892-1 [12]. Since the purpose of the tensile testing in this study is to give the same amount of plastic deformation as in the wire drawing process, the diameter is an important constraint so the formal tensile test specimen with a reduced section as shown in Figure 2.4.2 cannot be used. Instead, appropriate specifications are obtained by referring to the directions for preparation of unmachined tensile test specimen reported in the standard. Shape of an unmachined specimen can be seen in Figure 4.4.1.
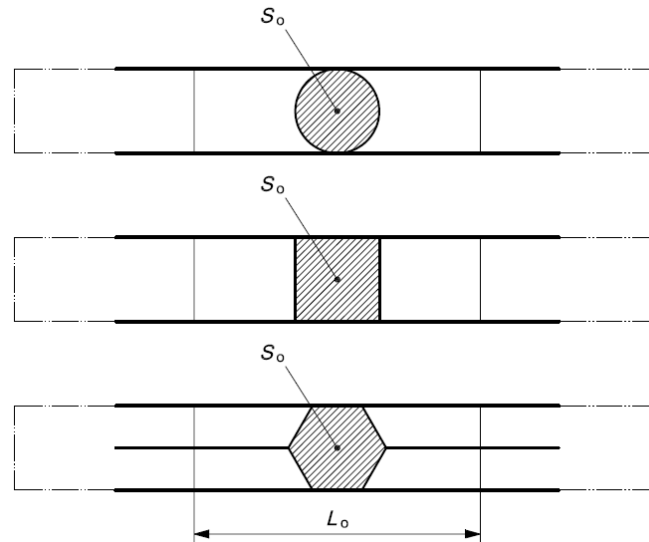
Figure 4.4.1 Unmachined tensile test specimen [12]

Due to the availability of the extensometer, for all diameters, non-proportional test pieces are used with a selected gauge length (L_0) of 50 mm. The parallel length (L_c), should not be less than $L_0 + b_0/2$ where b_0 is the original width, therefore the parallel length is selected 80 mm. Based on the restrictions of the testing machine total length (L_T) is selected 180 mm.

After the shape and the size of the specimens are decided, they are cut from the provided wire products by the use of abrasive disc cutter.

4.4.2 Procedure

After the specifications are determined and specimens are cut, gauge length is marked and they are inserted into the Alliance RT-100 tensile test machine one by one in order to perform proper tensile test for each specimen.

Tensile tests are carried as two different types of procedures. First type of procedure is called "break test" in which a tensile force is applied on the specimen until it breaks. Aim of the second procedure is to give the amount of deformation to the specimen up to a strain level which is identical to the deformation given in the wire drawing process and to compare the microstructural changes with their wiredrawn matches as well as their connection with the strain hardening properties of the materials. The strain level identical to the wire drawing deformation is calculated by the Equation 4.4.1 where $\varnothing_i$ is the initial diameter of the material to be drawn and $\varnothing_n$ is the final diameter of the drawn product.

24

For the break tests, one specimen for every diameter size (9, 8, 7 and 6.5 mm) is prepared for both AISI 316L and AISI 430 grade stainless steels. All the specimens are pulled until break down and stress and strain values are recorded with the aid of the software for the later use. After every test, elongation is measured from the difference of the marked gauge length.

Second type of procedure of the tensile tests is performed on the specimens, again for both AISI 316L and AISI 430 grades, up to a strain level which is calculated from the Equation 4.4.1 and can be referred as "loading-unloading tests". Calculated amount of strain levels to be given for each specimen are shown in the Table 4.4.1. Each strain level corresponds to an identical deformation taken by the wires during the wiredrawing process. There are eight specimens for both grades of steels which makes a total of sixteen specimens.

After calculation, those strain values are entered into the software as an input which controls the tensile test machine. After reaching every strain value the test is interrupted, stress is unloaded to 0 MPa and, if available, specimen started to be loading up to the next strain level. These tests result stress-strain graphs similar to the one seen in Figure 2.2.1(a).

$$\varepsilon = \ln\frac{\varnothing_i}{\varnothing_n}$$ **Equation 4.4.1**

Test	ε_1 (%)	ε_2 (%)	ε_3 (%)
9 to 8 mm	11.77	-	-
9 to 7 mm	25.13	-	-
9 to 6.5 mm	32.54	-	-
9 to 8 to 7 to 6.5 mm	11.77	25.13	32.54
8 to 7 mm	13.35	-	-
8 to 6.5 mm	20.76	-	-
8 to 7 to 6.5 mm	13.35	20.76	-
7 to 6.5 mm	7.41	-	-

Table 4.4.1 Step by step tensile test strain values for each specimen

Aim of these both tensile test procedures is to observe the trend of the strain hardening exponent (*n*) in the Equation 2.2.1, thus the strain hardening behavior of each type of stainless steel under different amounts of deformation. For this purpose, on every stress-strain graph obtained from tensile tests, a power function is fitted by considering the region between yield stress and necking point. Results of the tests will be discussed in Chapter 5.2.

4.5 EBSD Analyses

EBSD analyses are performed in order to understand microstructural changes and their relations with the hardening mechanisms in the materials. Tensile tested 9 mm samples (9 to 8 to 7 to 6.5 mm) from AISI 316L and AISI 430 grades of stainless steels are chosen to be undergone EBSD analysis in addition to the base 9 mm and wiredrawn 7 and 6.5 mm samples. Samples used in these analyses are all from the longitudinal-sections of the materials.

Small pieces from the tensile tested specimens are cut from the middle of the region which lies between the marked lines defining the gauge length. Cut pieces are then molded and back sides of the molds are grinded until the specimens were visible in order to assure the electrical conductivity and be able to perform EBSD analysis. Surfaces of the samples from tensile testing and molded samples used for microscopic examination are grinded and polished. Polishing is carried out step by step beginning with 6 μm diamond paste suspension followed by 3 μm and finally 1 μm. For this kind of analysis, surfaces of the samples must be very well polished as stated in the reference [13] hence an extra step for polishing is done with 0.2 μm colloidal silica suspension for approximately 1-1.5 hours.

After the preparation of the samples, they are inserted one by one into the chamber of the Zeiss branded SEM choosing the wiredrawing direction as the RD (rolling direction) which is defined in the reference system. Therefore ND and TD directions are become as in Figure 4.5.1 as a matter of course.

Analyses are performed on the specimens after choosing a proper area on their surfaces with a suitable magnification and resolution. The data acquired from the samples are pole figures, IPF's (inverse pole figures), ODF (orientation distribution function), CSL (coincidence site lattice) graphs and misorientation angle plots. These results are given and discussed in the Chapter 5.3.
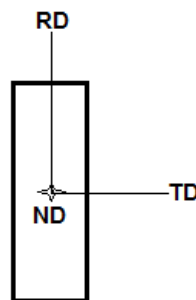
Figure 4.5.1 Reference system used in EBSD analyses

5 Results & Discussion

5.1 Microstructural Characterization

The results of metallographic investigations for the AISI 316L Austenitic Stainless Steel and AISI 430 Ferritic Stainless Steel before and after wire drawing are discussed in the following subsections.

5.1.1 AISI 316L Austenitic Stainless Steel

Cross-sectional micrograph of the 9 mm non-drawn sample as seen in Figure 5.1.1(a) has coarser grains and fewer twins relative to the wiredrawn samples with smaller diameters. The black point-like structures can be non-metallic inclusions [24], carbides or δ-ferrite [23]. Since they are uniformly dispersed throughout all of the micrographs of cross-sections as seen in Figure 5.1.1 and aligned to the direction of drawing which confirms that those particles are deformable as seen in Figure 5.1.2 so they are not concerned in this study and no further analysis are done to identify those black dot-like structures.

Figure 5.1.1(b) is the cross-sectional micrograph of the wiredrawn 8 mm sample, in which, decrease in the grain size and increase in the number of the twins can be observed due to the applied deformation.

Cross-sectional micrograph of the 7 mm wiredrawn sample can be seen in Figure 5.1.1(c). Going from 8 mm to 7 mm, increase in the deformation results; in higher reduction of the grain size and in the intensification of the twins.

As seen in Figure 5.1.1(d), the cross-sectional micrograph of the 6.5 mm wiredrawn sample shows finer grains due to the very high deformation.
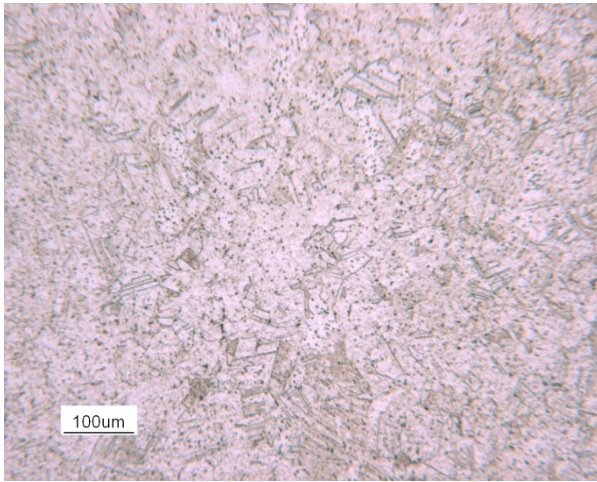
(a) 9 mm sample   **(b)** 8 mm sample
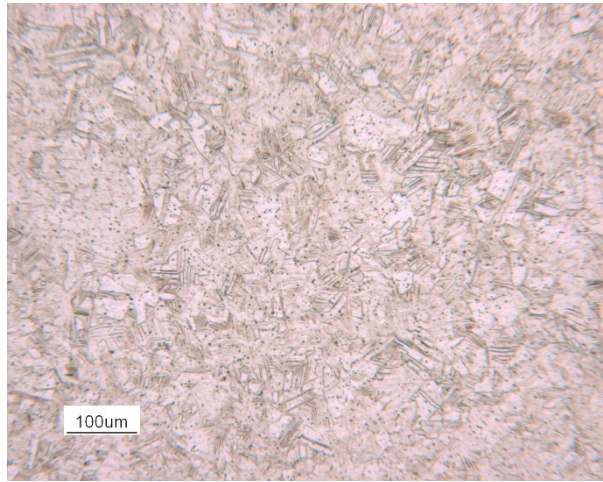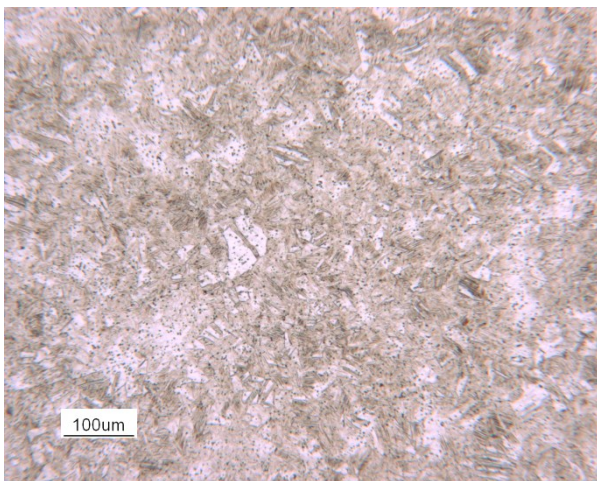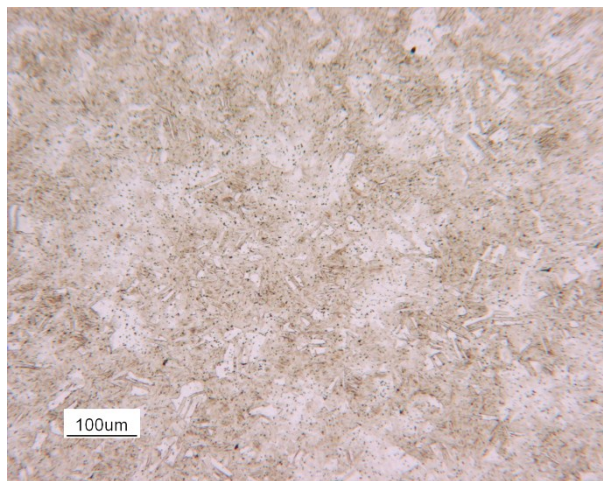
(c) 7 mm sample   **(d)** 6.5 mm sample

Figure 5.1.1 Microstructures of cross-sections of the AISI 316L Austenitic Stainless Steel samples for the diameter of (a) 9 mm (b) 8 mm (c) 7 mm (d) 6.5 mm, taken with 100x magnification under optical microscope

Longitudinal-section micrograph of the 9 mm non-drawn sample as seen in Figure 5.1.2(a) has again coarser grains and fewer twins relative to the wiredrawn samples with smaller diameters as in the cross-sectional micrographs. Inclusions are aligned parallel to the longitudinal direction confirming their deformability attitude.

Figure 5.1.2(b) is the longitudinal-section micrograph of the wiredrawn 8 mm sample, in which, due to the applied deformation, decrease in the grain size and increase in the number of the twins can be observed like in the cross-sectional micrograph as well as elongation of the grains parallel to the drawing direction. Slip planes can be clearly observed in the micrograph as dense thin lines and they are aligned diagonally [23].

Longitudinal-section micrograph of the 7 mm wiredrawn sample can be seen in Figure 5.1.2(c). Going from 8 mm to 7 mm, increase in the deformation results in a more

complicated microstructure with an even more reduction in the grain size and intensification of the slip lines.

As seen in Figure 5.1.2(d), the longitudinal-section micrograph of the 6.5 mm wiredrawn sample confirms again the more elongated and finer grain structure as seen in the cross-sectional one.

(a) 9 mm sample   **(b)** 8 mm sample
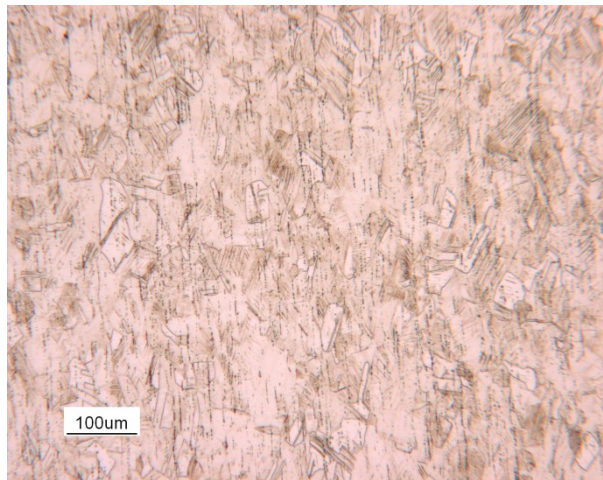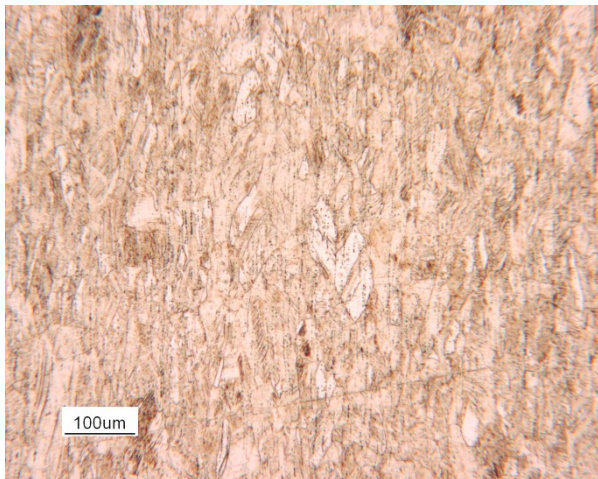
(c) 7 mm sample   **(d)** 6.5 mm sample

Figure 5.1.2 Microstructures of longitudinal-section of the AISI 316L Austenitic Stainless Steel samples for the diameter of (a) 9 mm (b) 8 mm (c) 7 mm (d) 6.5 mm, taken with 100x magnification under optical microscope
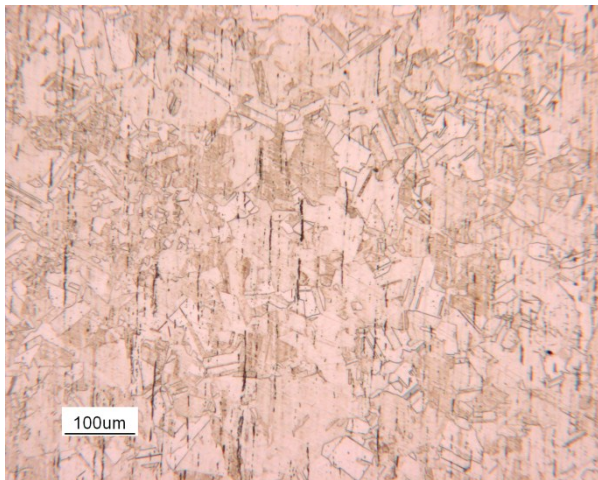
5.1.2 AISI 430 Ferritic Stainless Steel

Micrograph of the 9 mm non-drawn sample taken from the cross-sectional area which is seen in Figure 5.1.3(a) has coarser grains relative to the wiredrawn samples with smaller diameters. There are also black dot-like particles which are uniformly dispersed throughout all of the micrographs of cross-sections as seen in Figure 5.1.3 and aligned to the direction of drawing

which confirms that those particles are deformable as seen in Figure 5.1.4. Because of that they are not concerned in this study and no further analyses are done for these particles.

Figure 5.1.3(b) is the cross-sectional micrograph of the wiredrawn 8 mm sample showing a decrease in the grain size due to the applied deformation.

Cross-sectional micrograph of the 7 mm wiredrawn sample can be seen in Figure 5.1.3(c). Increased deformation going from 8 mm to 7 mm results in more reduction in the grain size.

As seen in Figure 5.1.3(d), the cross-sectional micrograph of the 6.5 mm wiredrawn sample shows the smaller sized grains among the other samples due to the very high amount of deformation.
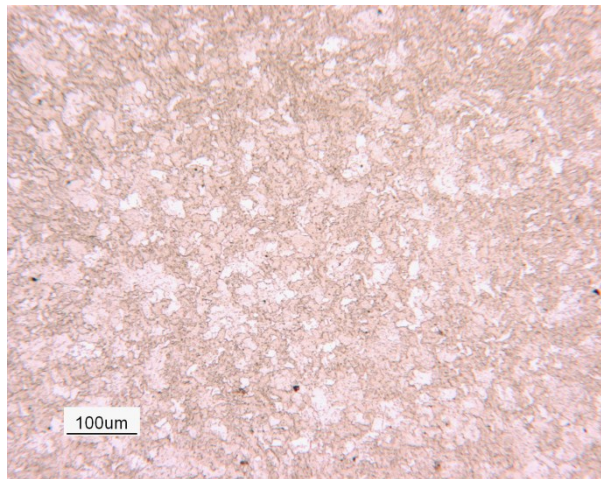
(a) 9 mm sample
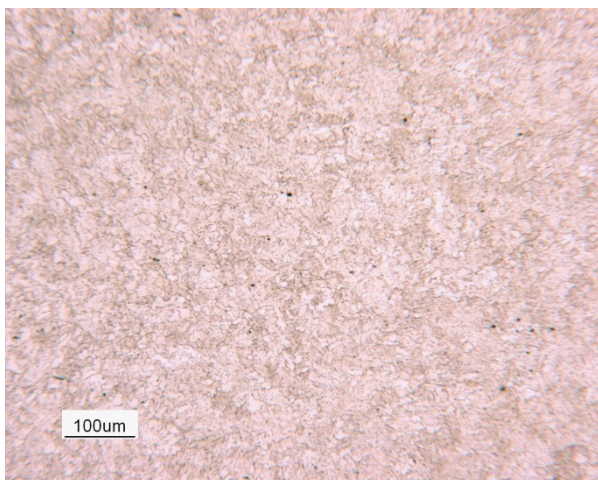
(b) 8 mm sample
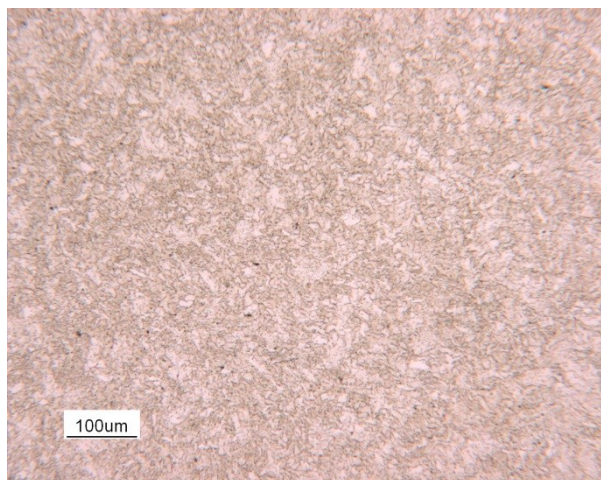
(c) 7 mm sample

(d) 6.5 mm sample

Figure 5.1.3 Microstructures of cross-sections of the AISI 430 Ferritic Stainless Steel samples for the diameter of (a) 9 mm (b) 8 mm (c) 7 mm (d) 6.5 mm, taken with 100x magnification under optical microscope

Micrograph of the 9 mm non-drawn sample taken from the longitudinal-section which is seen in Figure 5.1.4(a) has again coarser grains relative to the wiredrawn samples with smaller diameters as in the cross-sectional micrographs. Inclusions are aligned parallel to the longitudinal direction. Figure 5.1.4(b) is the longitudinal-section micrograph of the wiredrawn 8 mm sample showing a decrease in the grain size and elongation of the grains parallel to the drawing direction due to the applied deformation. Longitudinal-section micrograph of the 7 mm wiredrawn sample can be seen in Figure 5.1.4(c). Increased deformation going from 8 mm to 7 mm results in a more complicated microstructure with an even more reduction in the grain size and elongation of the grains. As seen in Figure 5.1.4(d), the longitudinal-section micrograph of the 6.5 mm wiredrawn sample, shows the smaller sized grains among the other samples due to the very high amount of deformation.
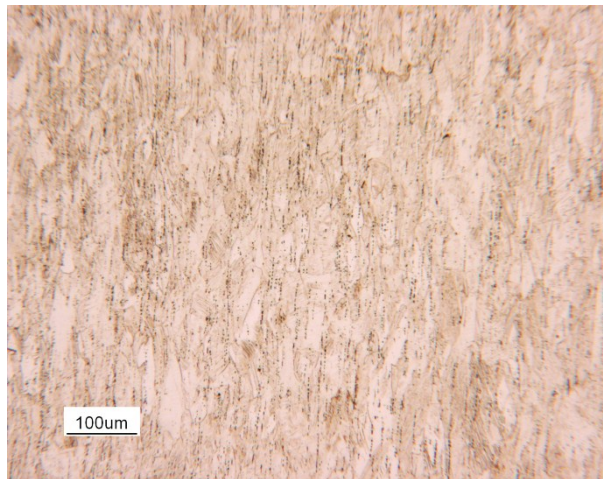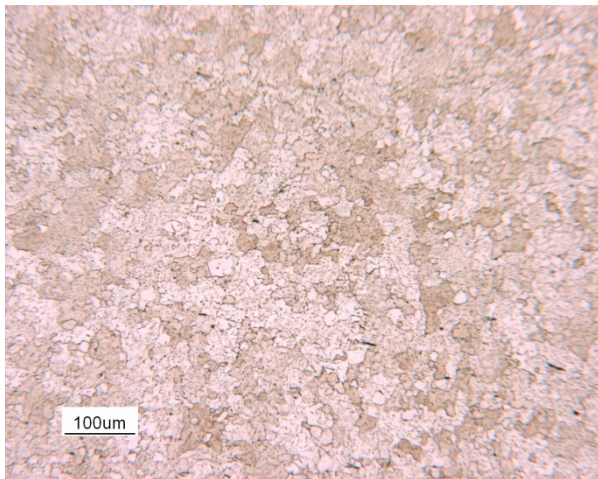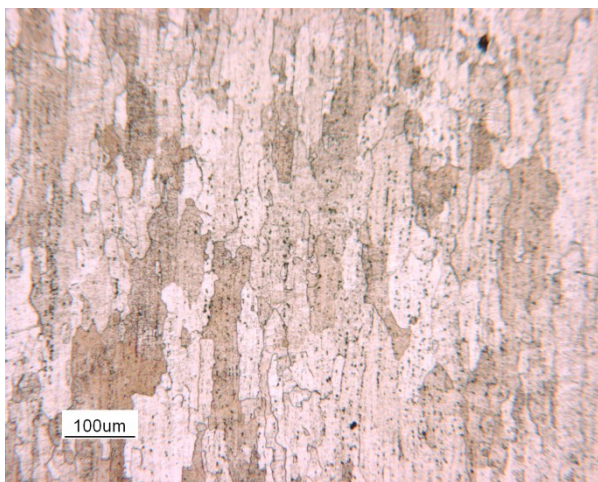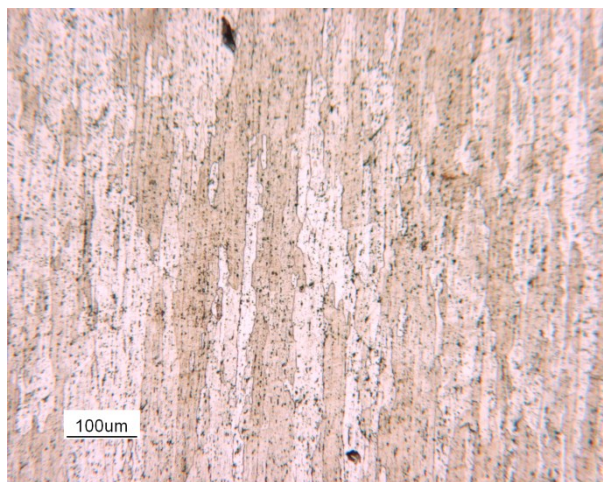
(a) 9 mm sample
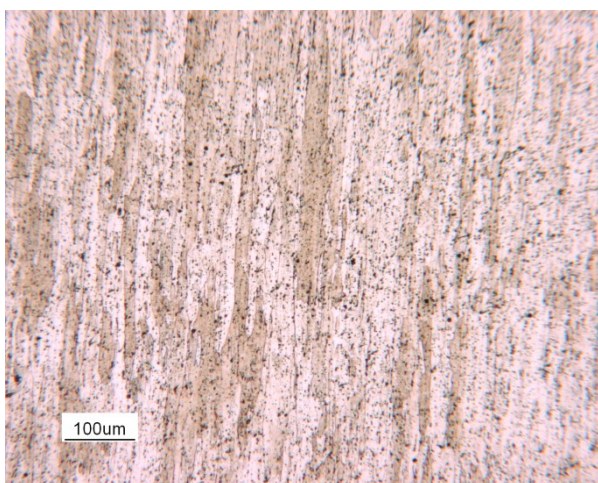
(b) 8 mm sample
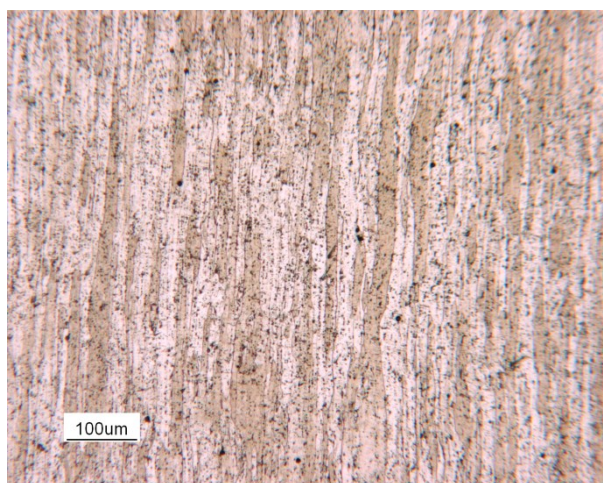
(c) 7 mm sample

(d) 6.5 mm sample

Figure 5.1.4 Microstructures of longitudinal-sections of the AISI 430 Ferritic Stainless Steel samples for the diameter of (a) 9 mm (b) 8 mm (c) 7 mm (d) 6.5 mm, taken with 100x magnification under optical microscope

5.2 Tensile Test

5.2.1 AISI 316L Austenitic Stainless Steel

The data obtained from the tensile tests are used to build the stress-strain diagrams. The stress-strain diagrams for the so called "break" tests of the 9 mm, 8 mm, 7 mm and 6.5 mm specimens are shown in Figure 5.2.1, Figure 5.2.2, Figure 5.2.3 and Figure 5.2.4 respectively. The stress-strain diagram of the so called "loading-unloading" test performed in three steps for the 9 mm austenitic specimen can be seen in Figure 5.2.5. The corresponding tables for the conditions and results of each test are given below the diagrams. The results of yield strength, UTS and strain hardening exponent (n) show same trends in all the tensile tests performed. Only the results of the break tests of 9 mm, 8 mm, 7 mm and 6.5 mm specimens and loading-unloading test of 9 mm specimen are given as representatives of all the test results.

The results of the break tests can be summarized as in the Table 5.2.1 and the results of the loading-unloading test are summarized in Table 5.2.2.

Specimen	Deformation (%)	Yield Strength (MPa)	UTS (MPa)	Strain Hardening Exponent (n)
9 mm	85.9	234	604	0.2126
8 mm	24.5	702	809	0.0158
7 mm	8.8	869	968	0.0389
6.5 mm	12.3	988	1070	0.0474

Table 5.2.1 Results of the break tests of AISI 316L austenitic stainless steel specimens

	Deformation (%)	Strain Hardening Exponent (n)
ε_1	11.78	0.2527
ε_2	25.13	0.2452
ε_3	32.54	0.1965

Table 5.2.2 Results of the loading-unloading test of AISI 316L austenitic stainless steel specimen

From the results of the break tests, it is observed that percent deformation is decreasing while going from 9 mm specimen to smaller diameter specimens as expected since they are already cold worked. The increase of the deformation percent on 6.5 mm specimen is due to a probable experimental error. Also the yield strength and the UTS of the specimens show an increasing trend due to the strain hardening caused by the cold deformation.

Experimental value of the strain hardening exponent (*n*) of 9 mm specimen of the base material is relatively high compared to the other wiredrawn specimens which indicates that 9 mm specimen will have a high increase in strength with a small amount of plastic deformation as it is confirmed in the stress-strain diagram shown in Figure 5.2.1. Going from the 9 mm specimen to the 8 mm wiredrawn specimen strain hardening exponent decreases dramatically while going from the 8 mm specimen to the 6.5 mm specimen, strain hardening exponents show an increasing trend.

As given in Table 5.2.2, the strain hardening exponents obtained from the loading-unloading test shows a decreasing trend which is due to the hardening during the test and it became difficult to obtain further strain hardening. Specimen tested in loading-unloading tensile test and specimens from provided drawn wires tested in break tests show a different trend for the strain hardening exponent (*n*).
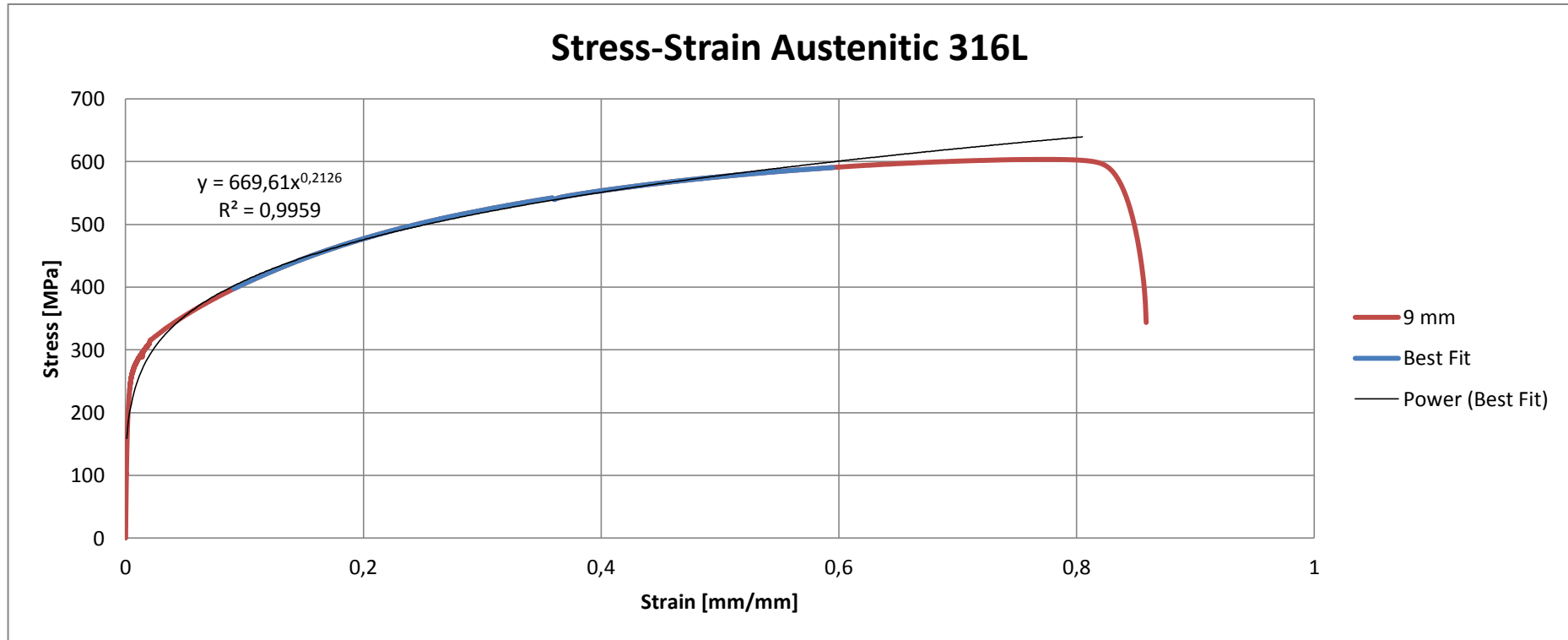
Figure 5.2.1 Stress-strain graph obtained from tensile testing of AISI 316L 9 mm specimen up to fracture

Name	Value	Units		Name	Value	Units
Test Speed	1.0	mm/min		**Peak Stress**	604	Mpa
Initial Diameter	9.00	mm		**Strain At Break**	85.9	%
Young's Modulus	188254	MPa		**Stress At Break**	344	Mpa
Rp02	234	MPa		**A%**	70.0	%

Table 5.2.3 Conditions and results of the tensile testing of AISI 316L 9 mm specimen
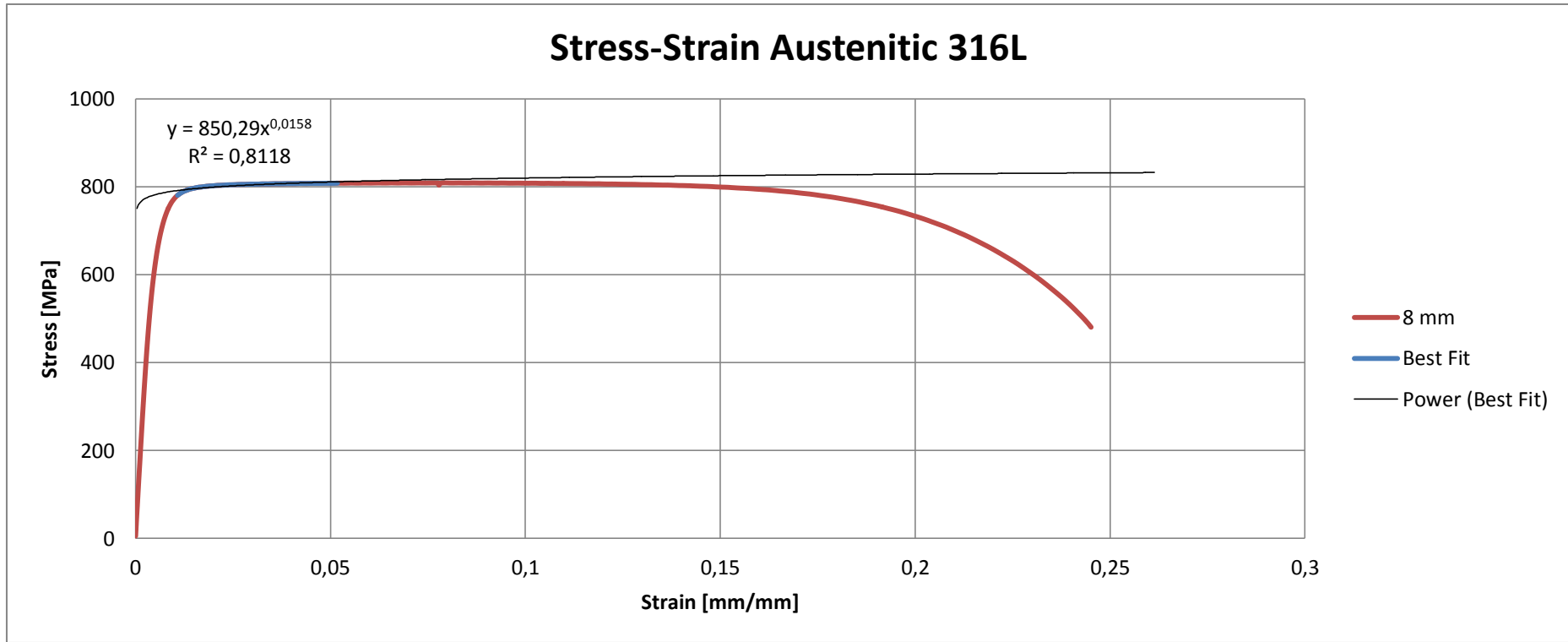
Figure 5.2.2 Stress-strain graph obtained from tensile testing of AISI 316L 8 mm specimen up to fracture

Name	Value	Units	Name	Value	Units
Test Speed	1.0	mm/min	**Peak Stress**	809	Mpa
Initial Diameter	8.00	mm	**Strain At Break**	24.5	%
Young's Modulus	152074	MPa	**Stress At Break**	481	Mpa
Rp02	702	MPa	**A%**	24.4	%

Table 5.2.4 Conditions and results of the tensile testing of AISI 316L 8 mm specimen
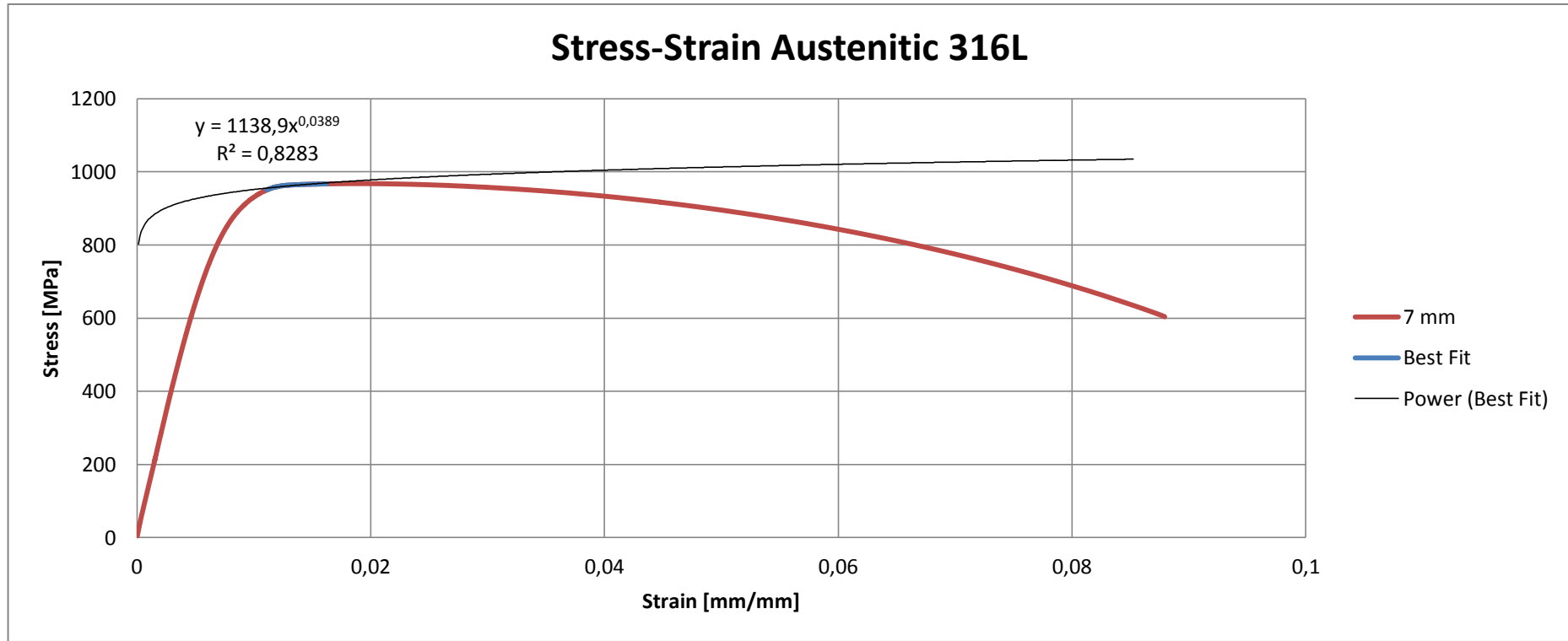
Figure 5.2.3 Stress-strain graph obtained from tensile testing of AISI 316L 7 mm specimen up to fracture

Name	Value	Units		Name	Value	Units
Test Speed	1.0	mm/min		**Peak Stress**	968	Mpa
Initial Diameter	7.00	mm		**Strain At Break**	8.8	%
Young's Modulus	143488	MPa		**Stress At Break**	604	Mpa
Rp02	869	MPa		**A%**	10.8	%

Table 5.2.5 Conditions and results of the tensile testing of AISI 316L 7 mm specimen
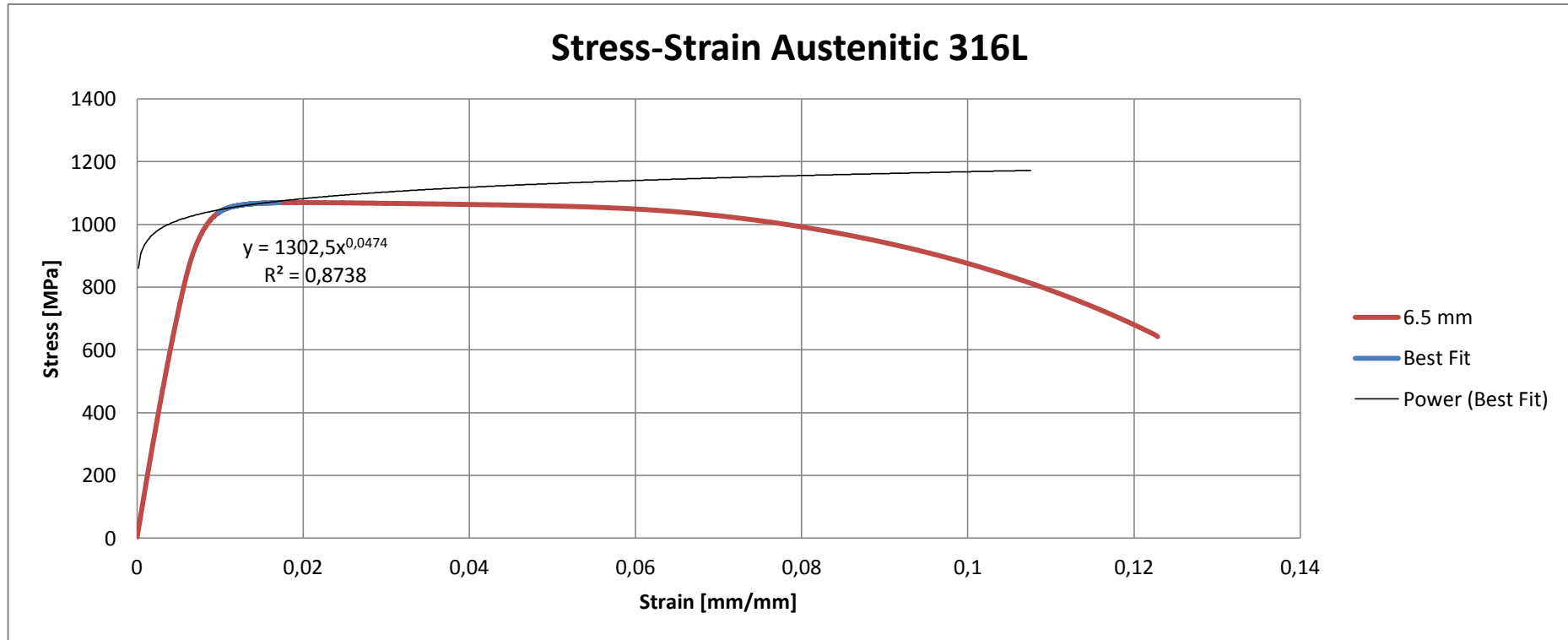
Figure 5.2.4 Stress-strain graph obtained from tensile testing of AISI 316L 6.5 mm specimen up to fracture

Name	Value	Units	Name	Value	Units
Test Speed	1.0	mm/min	**Peak Stress**	1070	Mpa
Initial Diameter	6.50	mm	**Strain At Break**	12.3	%
Young's Modulus	161382	MPa	**Stress At Break**	642	Mpa
Rp02	988	MPa	**A%**	12.0	%

Table 5.2.6 Conditions and results of the tensile testing of AISI 316L 6.5 mm specimen
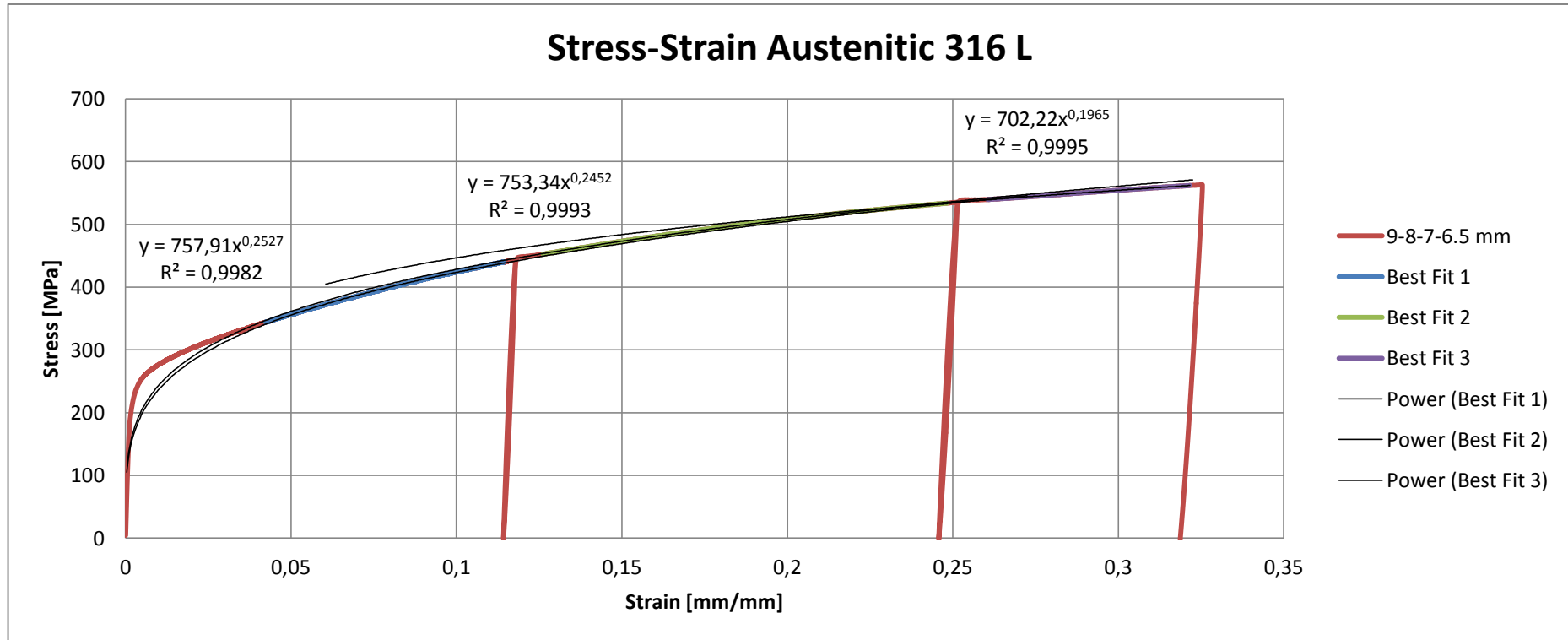
Figure 5.2.5 Stress-strain graph obtained from loading-unloading testing of AISI 316L 9 mm specimen up to 32.5% deformation, performed in 3 steps

Name	Value	Units	Name	Value	Units
Test Speed	1.0	mm/min	**Peak Stress**	-	Mpa
Initial Diameter	9.00	mm	ε_1	11.78	%
Young's Modulus	179334	MPa	ε_2	25.13	%
Rp02	239	MPa	ε_3	32.54	%

Table 5.2.7 Conditions and results of loading-unloading testing of AISI 316L 9 mm specimen up to 32.5% deformation, performed in 3 steps

5.2.2 AISI 430 Ferritic Stainless Steel

The data obtained from the tensile tests are used to build the stress-strain diagrams. The stress-strain diagrams for the so called "break" tests of the 9 mm, 8 mm, 7 mm and 6.5 mm specimens are shown in Figure 5.2.6, Figure 5.2.7, Figure 5.2.8 and Figure 5.2.9 respectively. The stress-strain diagram of the so called "loading-unloading" test performed in three steps for the 9 mm ferritic specimen can be seen in Figure 5.2.10. The corresponding tables for the conditions and results of each test are given below the diagrams. The results of yield strength, UTS and strain hardening exponent (n) show same trends in all the tensile tests performed. Only the results of the "break" tests of 9 mm, 8 mm, 7 mm and 6.5 mm specimens and "loading-unloading" test of 9 mm specimen are given as representatives of all the test results.

The results of the "break" tests can be summarized as in the Table 5.2.8 and the results of the "loading-unloading" test are summarized in Table 5.2.9.

Specimen	Deformation (%)	Yield Strength (MPa)	UTS (MPa)	Strain Hardening Exponent (n)
9 mm	39.7	226	423	0.1941
8 mm	13.4	533	582	0.0806
7 mm	11.9	582	623	0.0425
6.5 mm	9.6	623	685	0.1096

Table 5.2.8 Results of the break tests of AISI 430 ferritic stainless steel specimens

	Deformation (%)	Strain Hardening Exponent (n)
ε_1	11.78	0.2000
ε_2	25.13	0.0512
ε_3	32.54	-

Table 5.2.9 Results of the loading-unloading test of AISI 430 ferritic stainless steel specimen

From the results of the break tests, it is observed that percent deformation is decreasing while going from 9 mm specimen to smaller diameter specimens as expected since they are already cold worked. Also the yield strength and the UTS of the specimens show an increasing trend due to the strain hardening caused by the cold deformation.

Experimental value of the strain hardening exponent (n) of 9 mm specimen of the base material is relatively high compared to the other wiredrawn specimens, which indicates that 9

mm specimen will have a high increase in strength with a small amount of plastic deformation as it is confirmed in the stress-strain diagram shown in Figure 5.2.6. Going from the 9 mm specimen to the 7 mm wiredrawn specimen, strain hardening exponents show a decreasing trend on the other hand, going from the 7 mm specimen to the 6.5 mm specimen, strain hardening exponent increases. This increase is due to the possible breakdown of the grains into sub-grains which allow further increase in strength with an applied deformation.

As given in Table 5.2.9, the strain hardening exponents obtained from the loading-unloading test shows the value of the strain hardening exponent is decreased going from step 1 (9 mm to 8 mm) to step 2 (8 mm to 7 mm). Since the necking of the specimen started during step 2, n value of step 3 (7 mm to 6.5 mm) cannot be determined. If the necking had not occurred during the entire test, it would also be expected to have a decreasing trend for step 3.

Stress-Strain Ferritic 430

$y = 620{,}05x^{0,1941}$
$R^2 = 0{,}9867$

Figure 5.2.6 Stress-strain graph obtained from tensile testing of AISI 430 9 mm specimen up to fracture

Name	Value	Units	Name	Value	Units
Test Speed	1.0	mm/min	**Peak Stress**	423	Mpa
Initial Diameter	9.00	mm	**Strain At Break**	39.7	%
Young's Modulus	175310	MPa	**Stress At Break**	166	Mpa
Rp02	226	MPa	**A%**	40.0	%

Table 5.2.10 Conditions and results of the tensile testing of AISI 430 9 mm specimen

Figure 5.2.7 Stress-strain graph obtained from tensile testing of AISI 430 8 mm specimen up to fracture

Name	Value	Units	Name	Value	Units
Test Speed	1.0	mm/min	Peak Stress	582	Mpa
Initial Diameter	8.00	mm	Strain At Break	13.4	%
Young's Modulus	155755	MPa	Stress At Break	265	Mpa
Rp02	533	MPa	A%	13.0	%

Table 5.2.11 Conditions and results of the tensile testing of AISI 430 8 mm specimen

Stress-Strain Ferritic 430

$y = 755{,}05x^{0{,}0425}$

$R^2 = 0{,}8098$

Legend:
- 7 mm
- Best Fit
- Power (Best Fit)

Stress [MPa] (y-axis: 0 to 800)
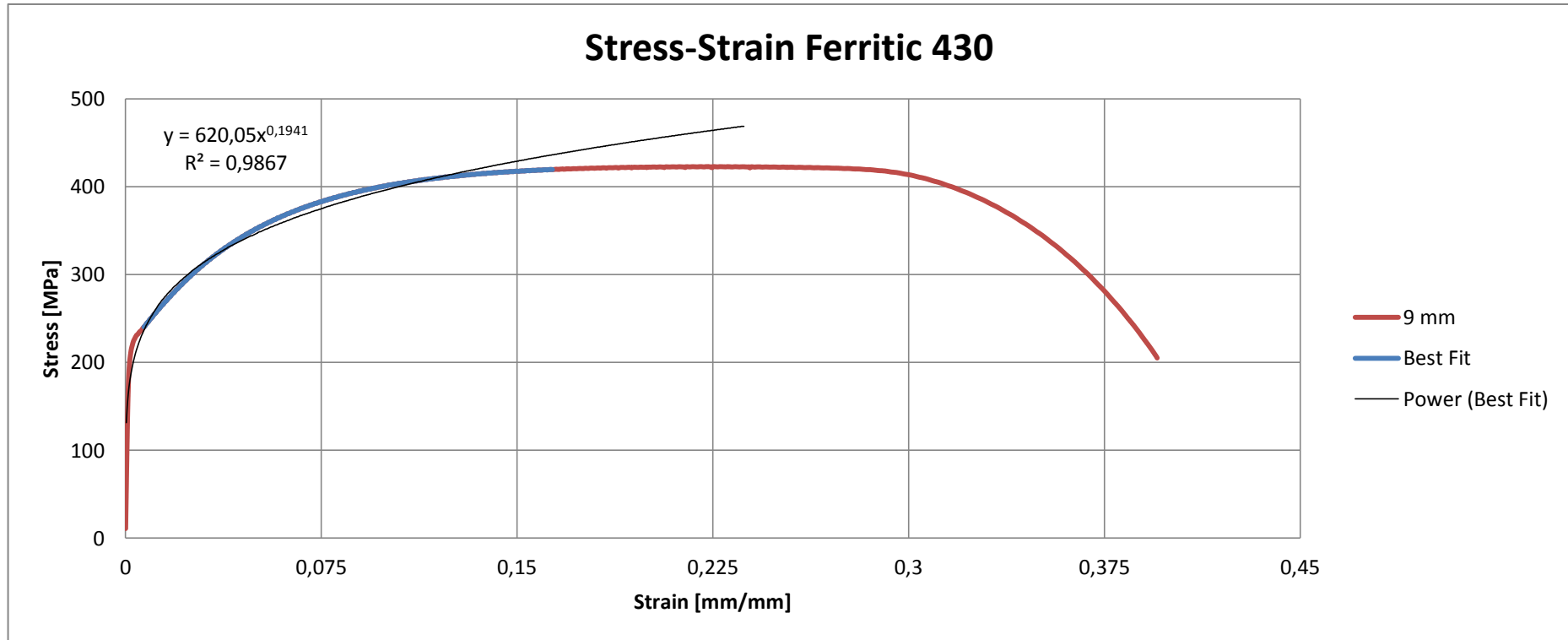Strain [mm/mm] (x-axis: 0 to 0,14)

Figure 5.2.8 Stress-strain graph obtained from tensile testing of AISI 430 7 mm specimen up to fracture

Name	Value	Units	Name	Value	Units
Test Speed	1.0	mm/min	**Peak Stress**	623	Mpa
Initial Diameter	7.00	mm	**Strain At Break**	11.9	%
Young's Modulus	219374	MPa	**Stress At Break**	306	Mpa
Rp02	582	MPa	**A%**	11.0	%

Table 5.2.12 Conditions and results of the tensile testing of AISI 430 7 mm specimen
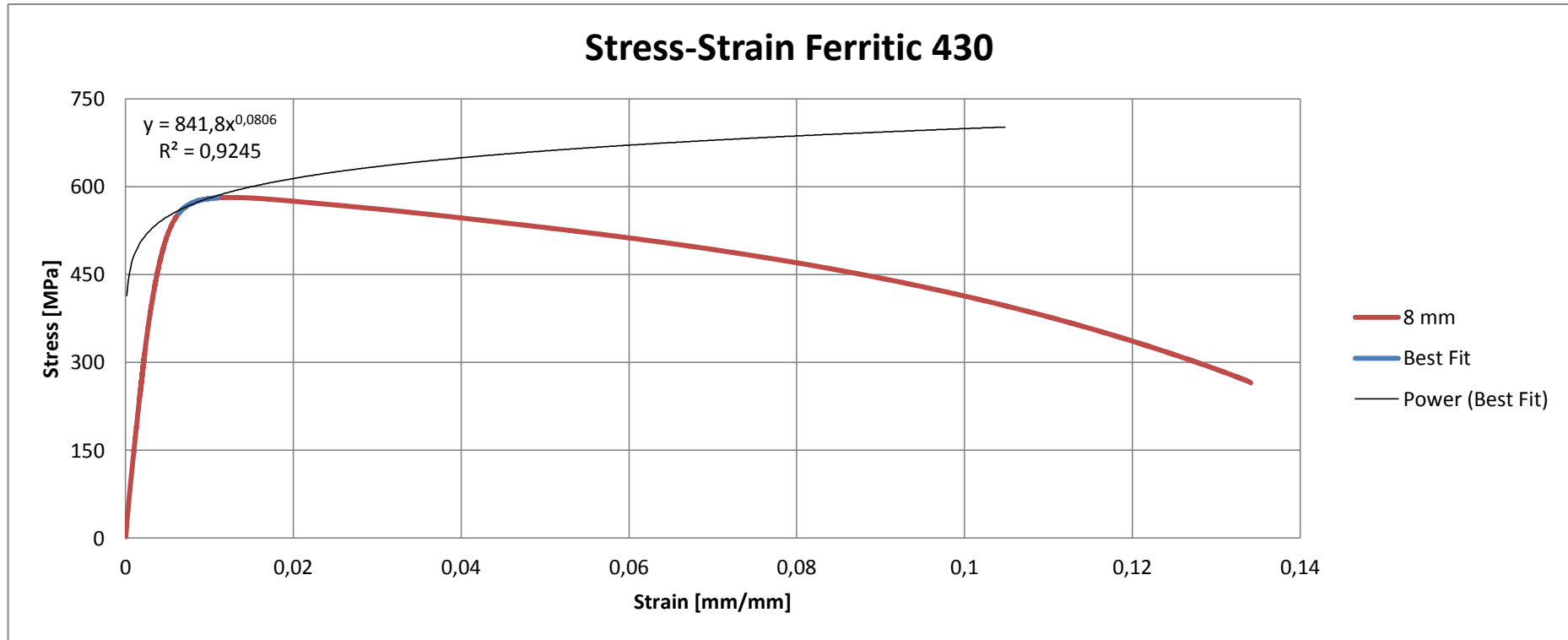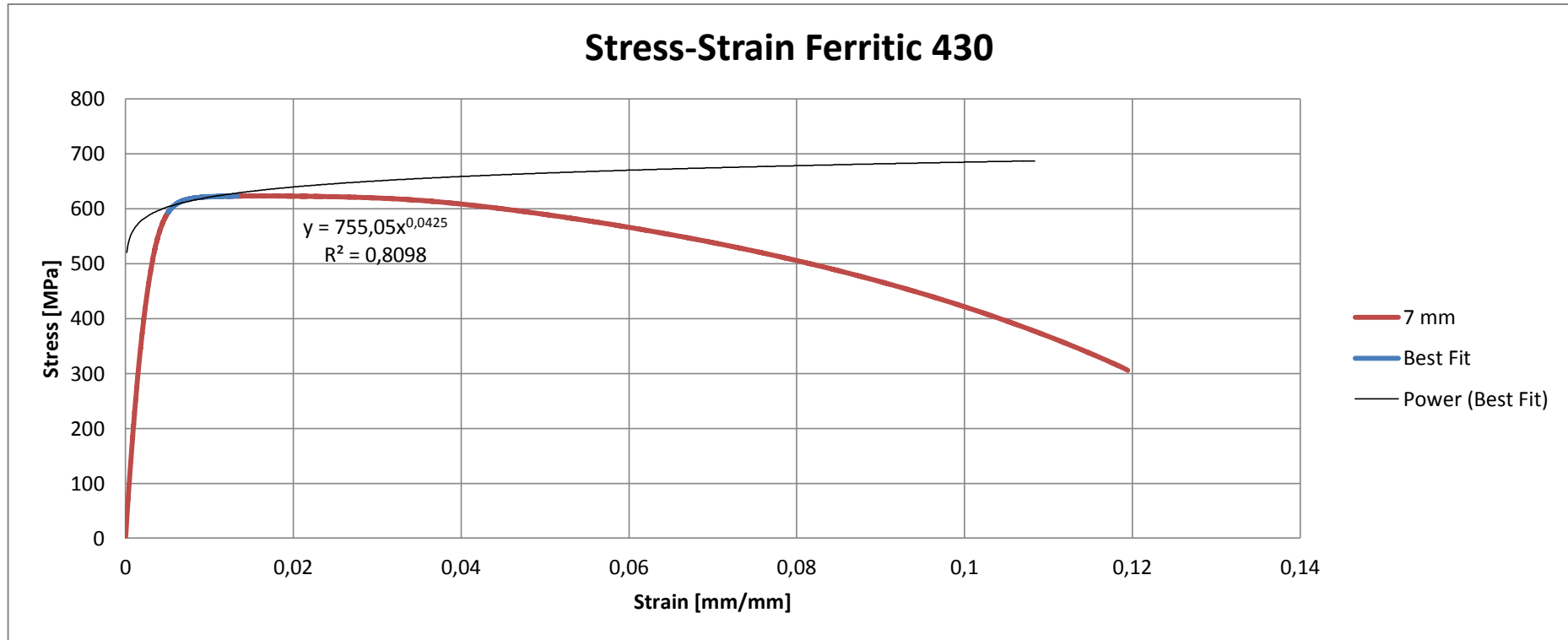
43
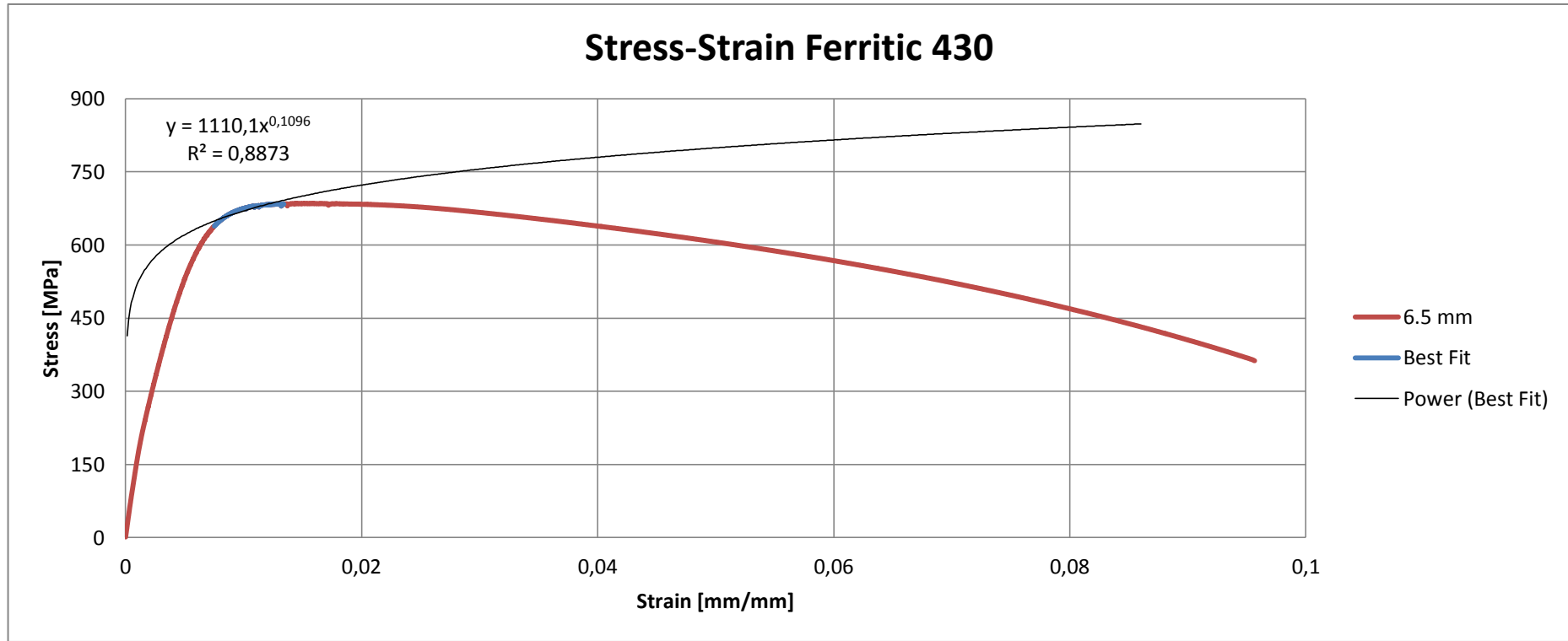
Figure 5.2.9 Stress-strain graph obtained from tensile testing of AISI 430 6.5 mm specimen up to fracture

Name	Value	Units	Name	Value	Units
Test Speed	1.0	mm/min	**Peak Stress**	685	Mpa
Initial Diameter	9.00	mm	**Strain At Break**	9.6	%
Young's Modulus	188254	MPa	**Stress At Break**	358	Mpa
Rp02	623	MPa	**A%**	8.0	%

Table 5.2.13 Conditions and results of the tensile testing of AISI 430 6.5 mm specimen

Stress-Strain Ferritic 430

$y = 654{,}13x^{0,2}$
$R^2 = 0{,}9955$

$y = 469{,}48x^{0,0512}$
$R^2 = 0{,}9618$

- 9-8-7-6.5 mm
- Best Fit 1
- Best Fit 2
- Power (Best Fit 1)
- Power (Best Fit 2)

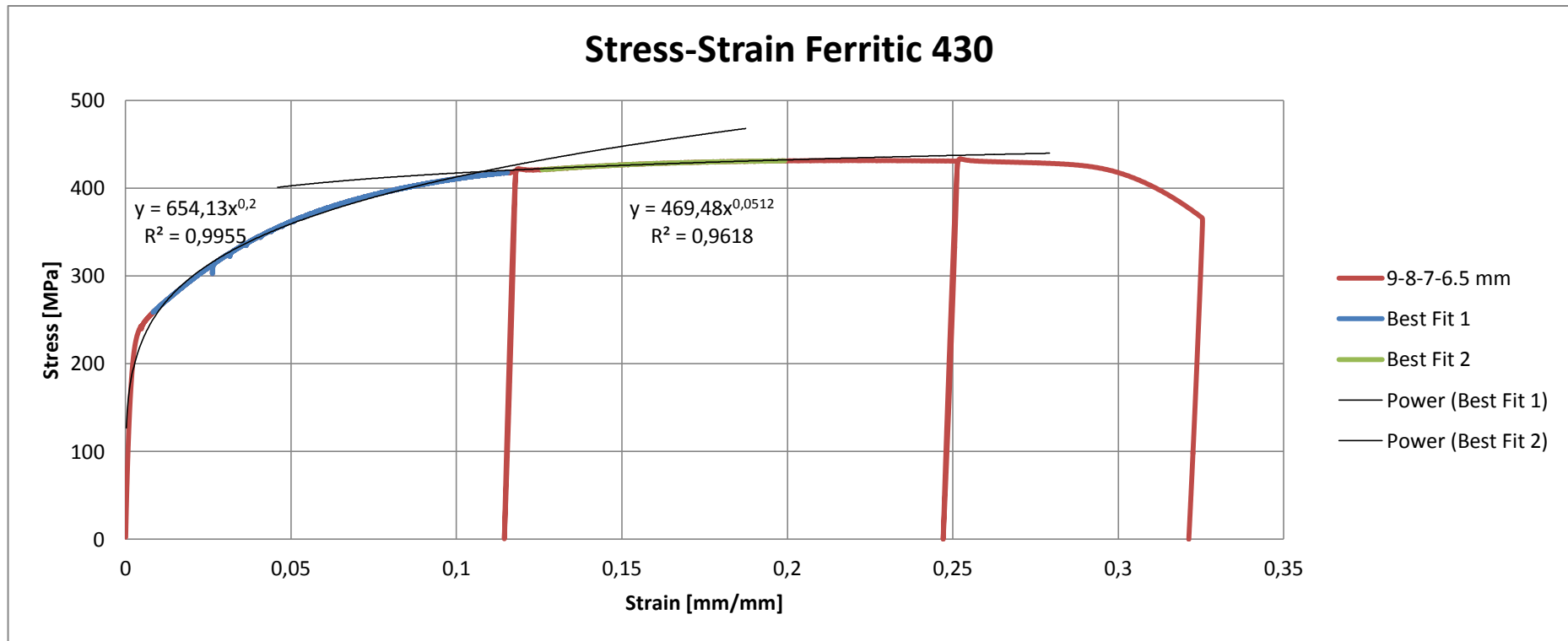**Figure 5.2.10 Stress-strain graph obtained from tensile testing of AISI 430 9 mm specimen up to 32.5% deformation, performed in 3 steps.**

Name	Value	Units	Name	Value	Units
Test Speed	1.0	mm/min	**Peak Stress**	434	Mpa
Initial Diameter	9.00	mm	ε_1	11.78	%
Young's Modulus	137074	MPa	ε_2	25.13	%
Rp02	235	MPa	ε_3	32.54	%

Table 5.2.14 Conditions and results of loading-unloading testing of AISI 430 9 mm specimen up to 32.5% deformation, performed in 3 steps

5.3 EBSD

5.3.1 AISI 316L Austenitic Stainless Steel

Pole figures of {1,0,0} and {1,1,1} obtained from the EBSD analyses for austenitic samples are shown in Figure 5.3.1 and Figure 5.3.2, respectively. It can be clearly seen in Figure 5.3.1(a) and Figure 5.3.2(a) that there is no preferential texture in the 9 mm base sample, proven by the homogenous dispersion of the plane projections. Figure 5.3.1(b) and Figure 5.3.2(b) show the pole figures of 7 mm sample which is cold deformed by wire drawing process. Formation of a fiber texture caused by wire drawing and alignment of both {1,0,0} and {1,1,1} perpendicular to the RD can be seen as expected for a FCC crystal structure [15]. With the increase of the deformation fiber texture becomes more pronounced and there is an intensification of the alignment of both {1,0,0} and {1,1,1} perpendicular to the RD.

Figure 5.3.1(d) and Figure 5.3.2(d) show the pole figure of the {1,0,0} and {1,1,1} respectively for the tensile tested sample. Evolution of the fiber texture and the alignment of the both {1,0,0} and {1,1,1} perpendicular to the RD are also confirmed by pole figures of the tensile tested sample. There is a slight difference between the pole figures of wiredrawn and tensile tested samples. In the tensile testing, the only force acting on the specimen is the uniaxial tensile force and the difference between the pole figures of wiredrawn and tensile tested samples is due to the additional die pressure to the tensile force acting on the wire during the drawing process.

Additionally, strain rate applied in the tensile testing is relatively low compared to the drawing process. This explains the higher intensification of {1,1,1} in the 6.5 mm sample than in the tensile tested sample as seen in Figure 5.3.2(c) and Figure 5.3.2(d).
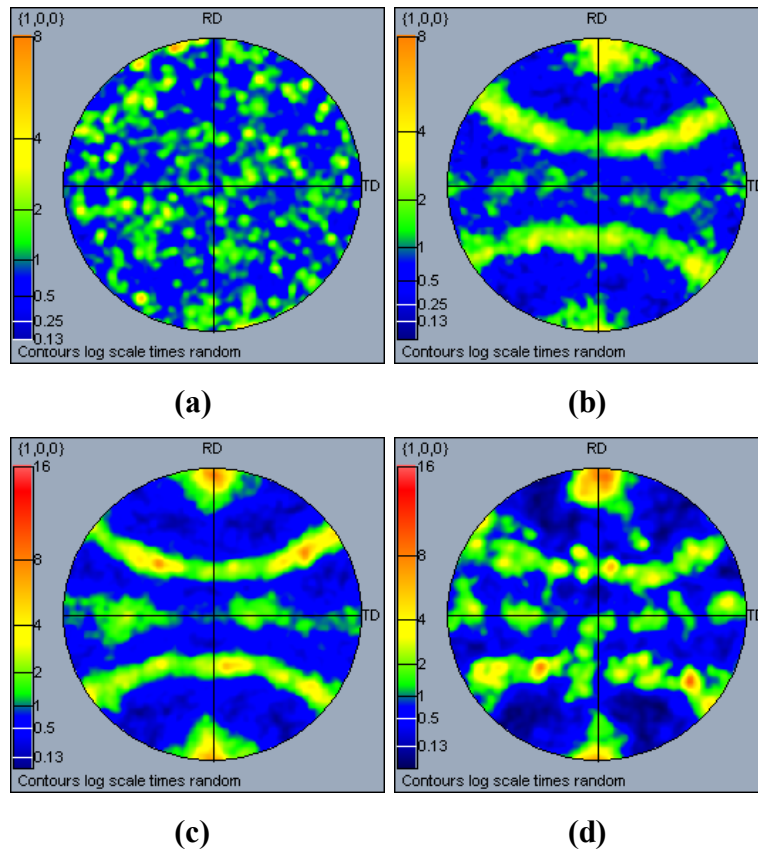
Figure 5.3.1 Pole figures of {1,0,0} obtained from EBSD analyses for AISI 316L (a) 9 mm (b) 7 mm (c) 6.5 mm (d) tensile tested sample
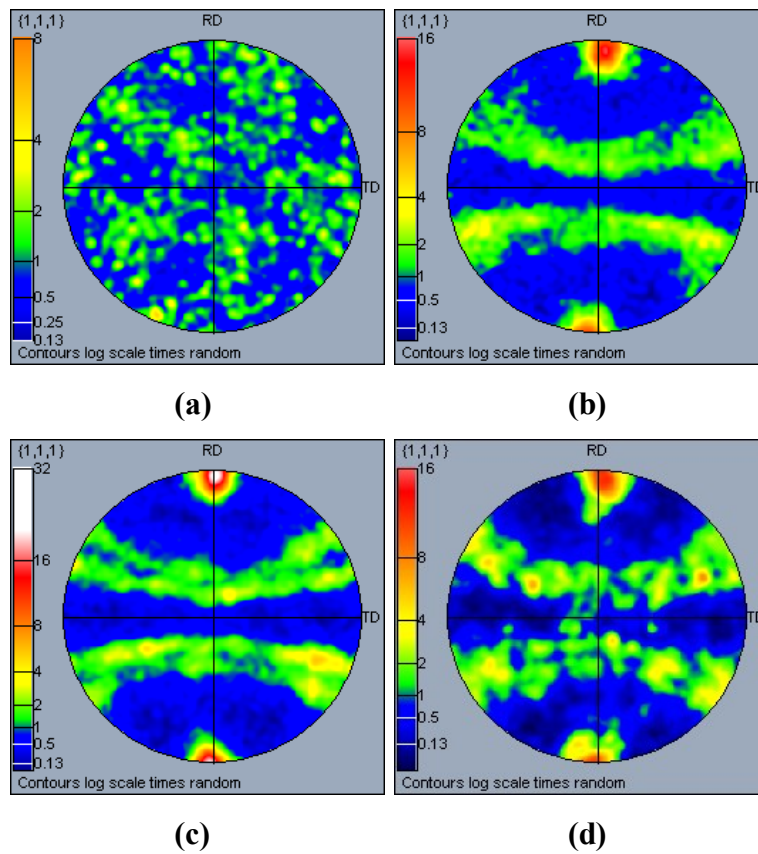

Figure 5.3.2 Pole figures of {1,1,1} obtained from EBSD analyses for AISI 316L (a) 9 mm (b) 7 mm (c) 6.5 mm (d) tensile tested sample

Inverse pole figures of RD obtained from EBSD analyses for austenitic samples are shown in Figure 5.3.3. Figure 5.3.3(a) confirms that there is no preferential orientation in the 9 mm sample as the pole figures. In Figure 5.3.3(b), it can be seen that crystallographic directions [001] and [111] are aligned parallel to the RD. 7 mm sample is behaving like a threshold and with the increasing deformation alignment of [111] parallel to RD tends to dominate the alignment of [001] and the material tends to align only [111] to the RD in the 6.5 mm sample as seen in Figure 5.3.3(c). There are still many grains in the material with the alignment of [001] parallel to the RD but the new step of the deformation mostly aligns the [111] parallel to the RD since the difference of the intensities between [111] and [001] seems to increase in the IPF.

Figure 5.3.3(d) shows the IPF of the RD for the tensile tested sample of AISI 316L austenitic stainless steel. Again due to the differences of the processes of the tensile testing and wire drawing, as explained above, tensile tested sample shows an intermediate behavior between 7 mm and 6.5 mm samples. It can be seen that the intensity of alignment of [111] started to dominate the alignment of [001] but difference in the intensities are not as high as in the 6.5 mm sample.
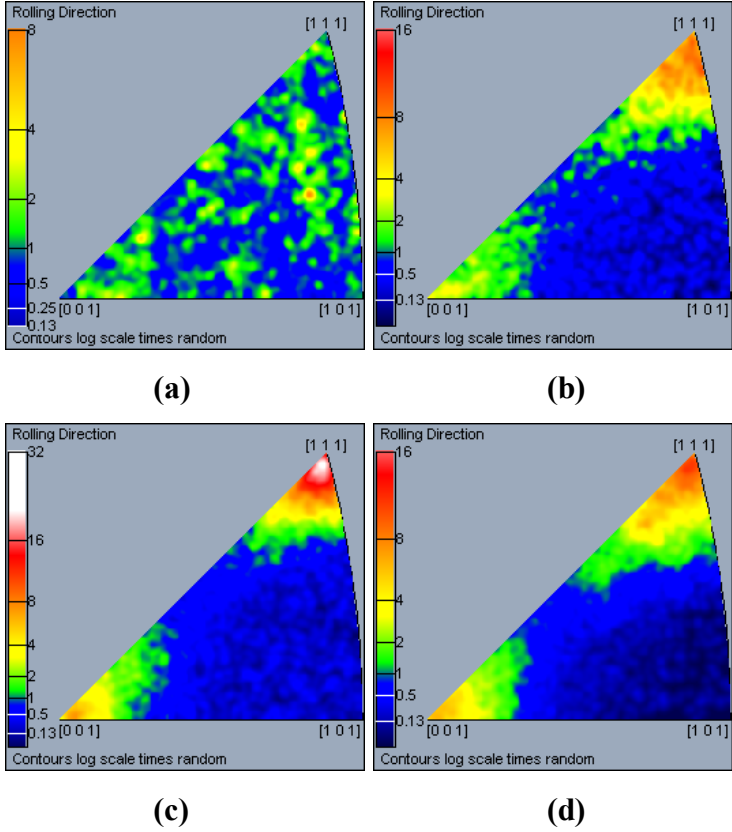

Figure 5.3.3 Inverse polar figures parallel to rolling direction for AISI 316L (a) 9 mm (b) 7 mm (c) 6.5 mm and (d) tensile tested sample obtained from EBSD analyses

Figure 5.3.4 shows the ODF plot of the 9 mm sample of AISI 316L austenitic stainless steel. There is the presence of Goss (G), Brass (B), Cube and Rotated Cube textures.
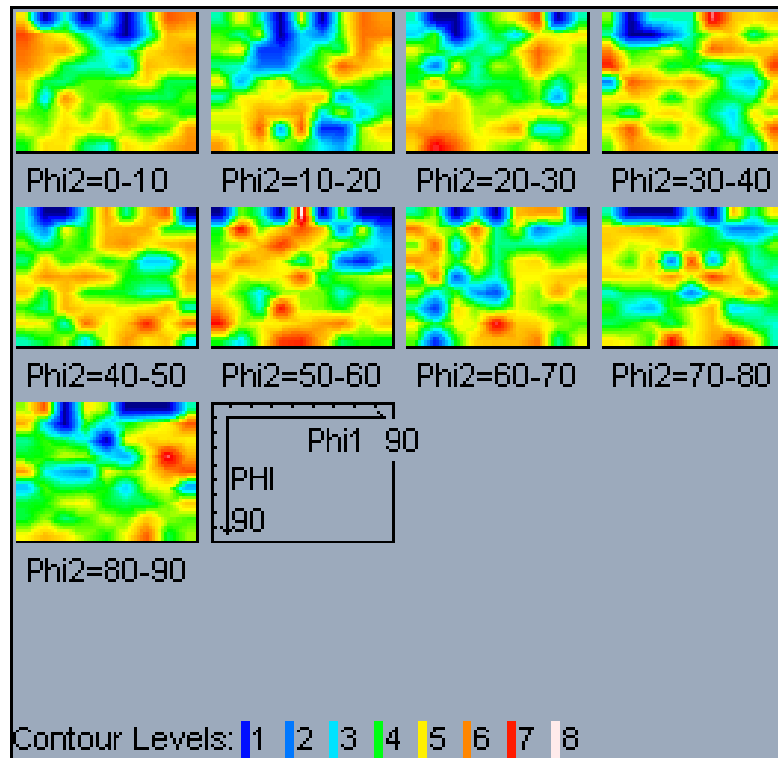

Figure 5.3.4 ODF plots for AISI 316L 9 mm sample with changing φ_2 Euler angles

ODF plots of 7 mm and 6.5 mm wiredrawn samples are shown in Figure 5.3.5 and Figure 5.3.6, respectively. Intensification of Rotated Cube {001}<101> and Brass {011}<112> textures are observed by the increase of the deformation. Also formation and intensification of S {123}<634> texture by the increase of deformation can be seen in the ODF plots. However, the Goss texture tends to disappear and tries to transform in another texture like Copper {112}<111> texture. While going from 7 mm sample to 6.5 mm sample the link between Goss and Brass, which is the α-fiber, tends to disappear and transform into a strong β-fiber.

The transformation of the α-fiber to the β-fiber may have a connection with the gradual increase of the experimental values of strain hardening exponent (*n*) reported in the Table 5.2.1.
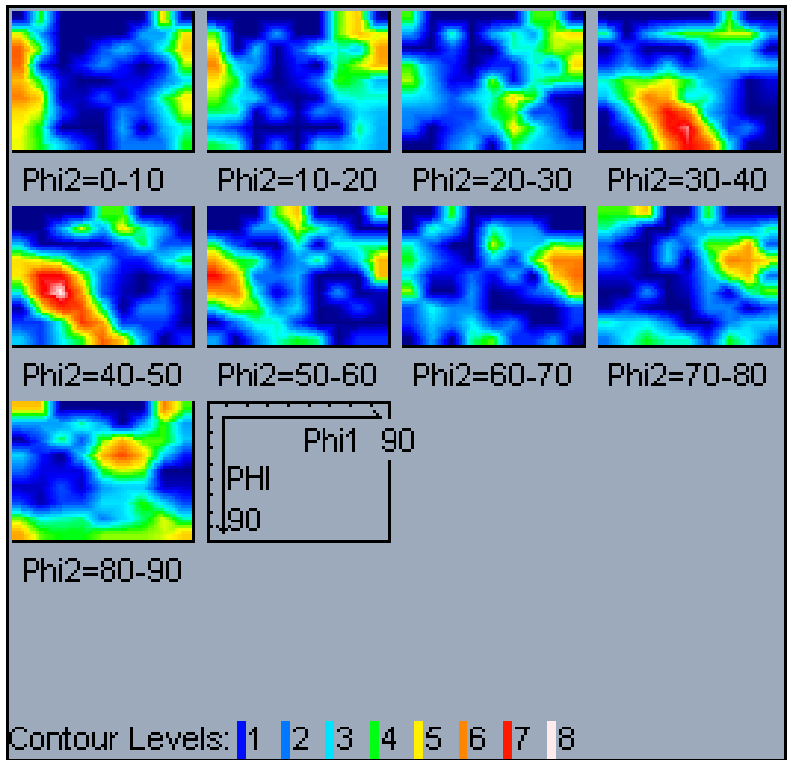
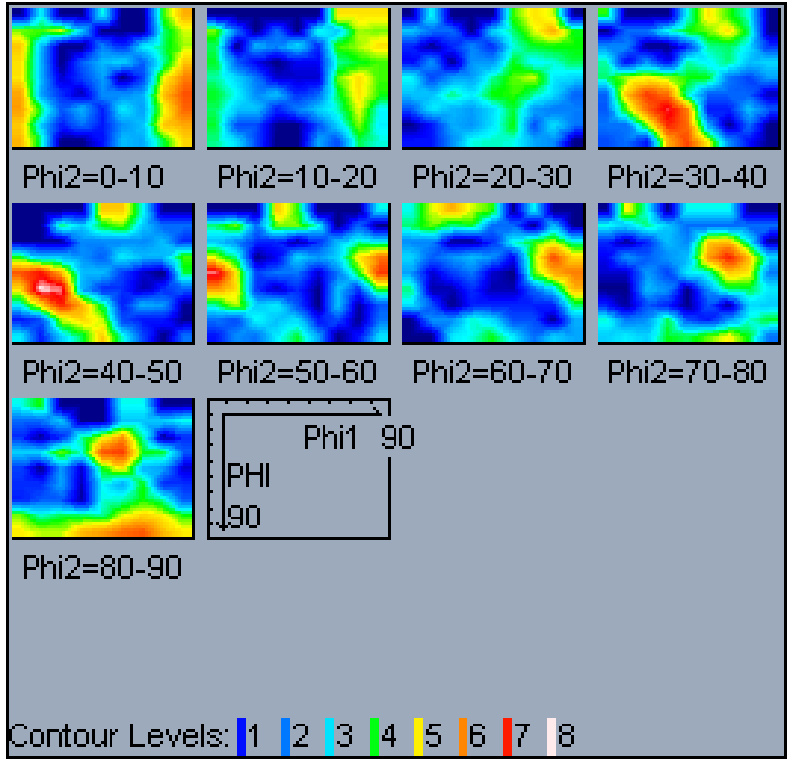**Figure 5.3.5 ODF plots for AISI 316L 7 mm sample with changing φ_2 Euler angles**

Figure 5.3.6 ODF plots for AISI 316L 6.5 mm sample with changing φ_2 Euler angles

The tensile tested sample has similar texture formation as the wiredrawn samples as seen in Figure 5.3.7. However, due to the differences between tensile testing and wiredrawing, evolution and intensification of the textures in the tensile tested sample is between the 7 mm and 6.5 mm drawn samples.
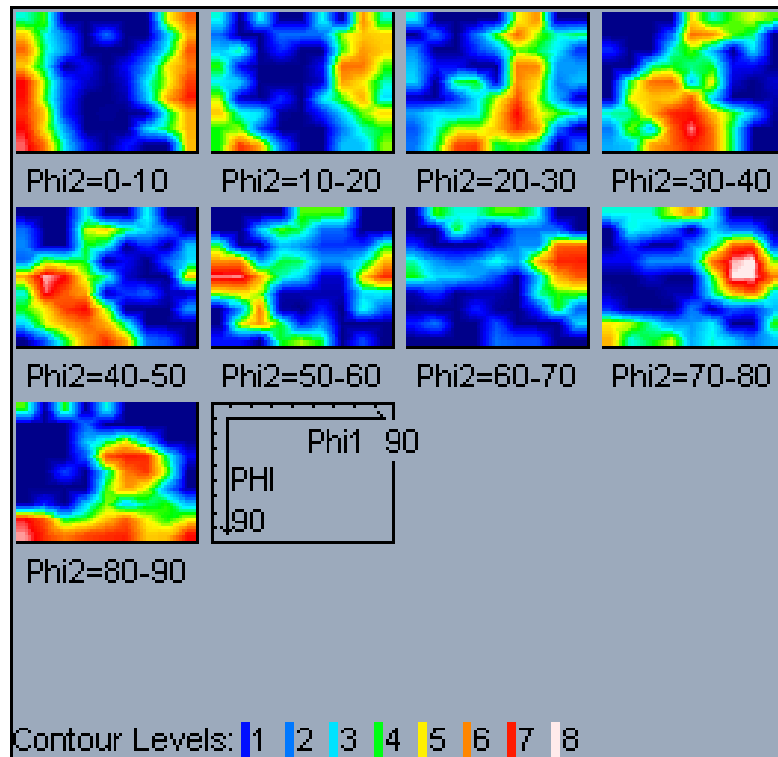

Figure 5.3.7 ODF plots for AISI 316L tensile tested sample with changing φ_2 Euler angles

Figure 5.3.8 shows the coincidence site lattice graphs of austenitic stainless steel samples. High frequency of Σ3 special boundaries can be observed which indicates that there are high numbers of twins in the material. 9 mm sample shows the highest number of Σ3 special boundaries compared to the other samples as seen in Figure 5.3.8(a). For the 7 mm sample seen in the Figure 5.3.8(b), the CSL number of Σ3's decreased, featured by two different directions that have been activated by plastic deformation. In the CSL graph of 6.5 mm sample seen in Figure 5.3.8(c), the number of Σ3's are increased again similar to the strain hardening exponent (*n*).
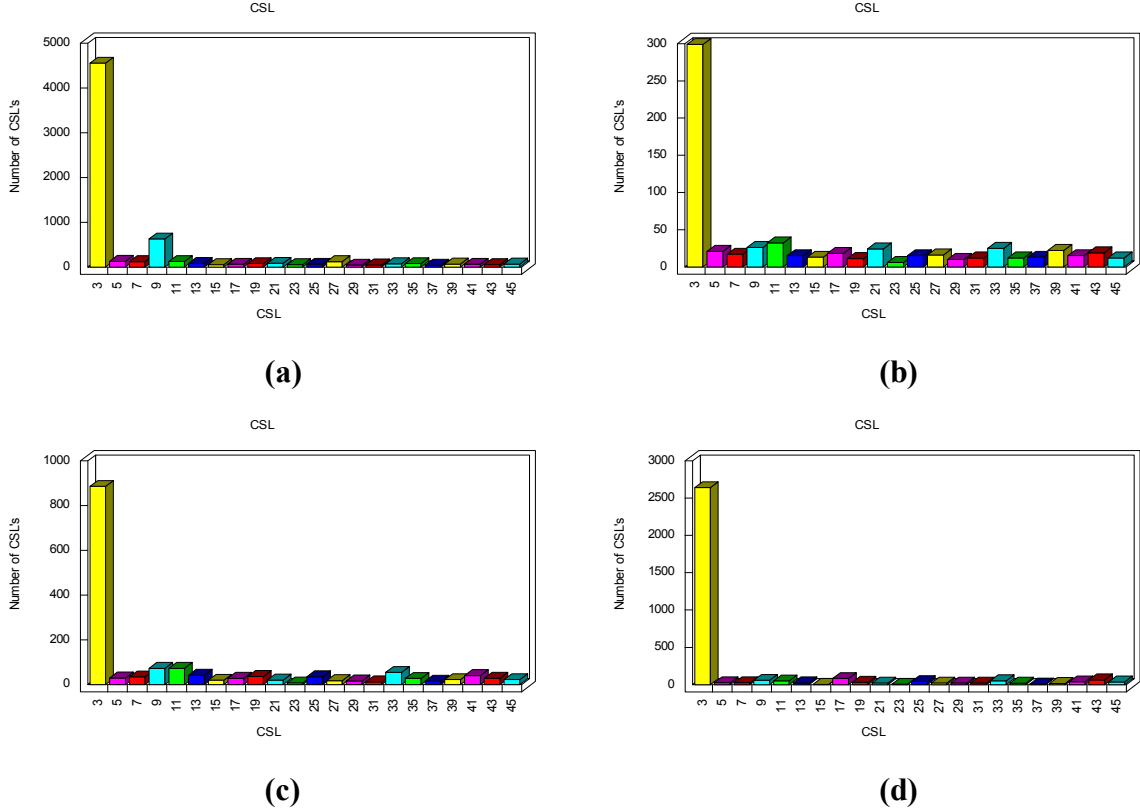

Figure 5.3.8 CSL graphs for the AISI 316L (a) 9 mm (b) 7 mm (c) 6.5 mm (d) tensile tested samples

Distributions of misorientation angles of boundaries for the austenitic samples are shown in Figure 5.3.9. It is observed that in the 9 mm base sample misorientations are mostly at high angles (>50°). With the deformation, the misorientations tend to disperse through lower angles. Increase in the amount of deformation leads to the concentration of the misorientations at low angles (<10°).
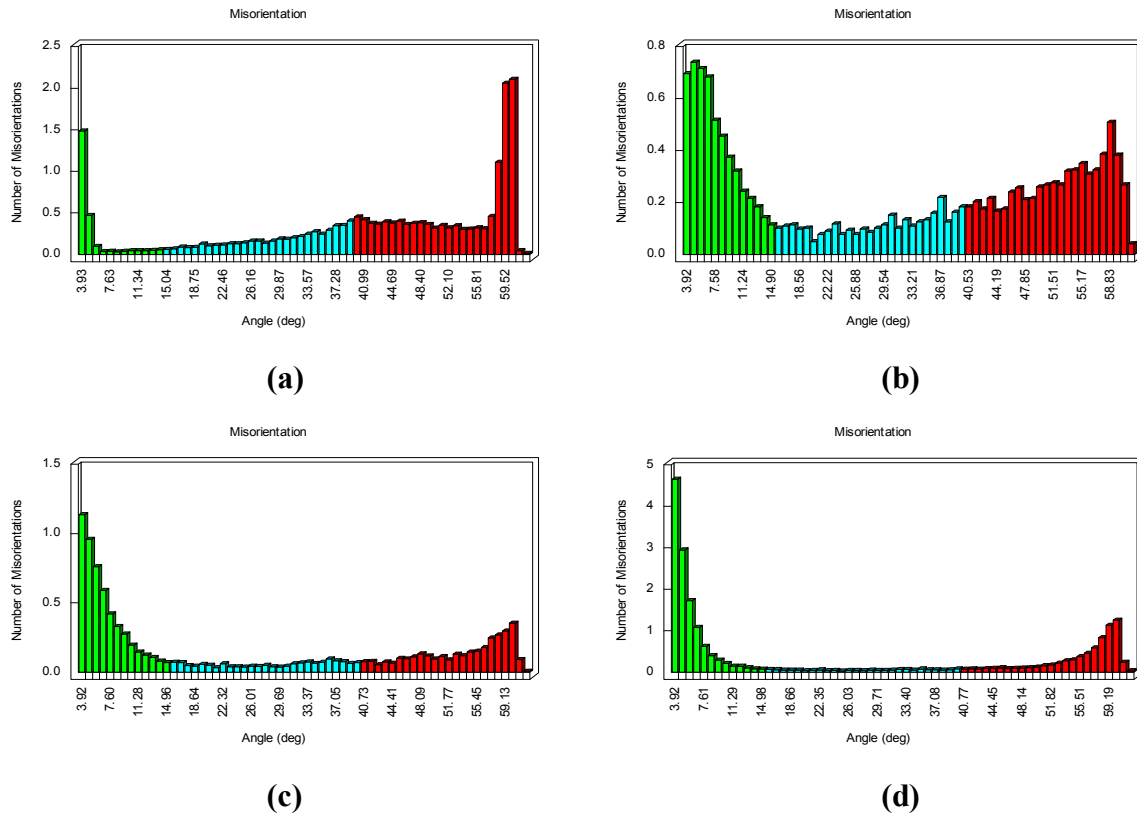

Figure 5.3.9 Misorientation graphs for the AISI 316L (a) 9 mm (b) 7 mm (c) 6.5 mm (d) tensile tested samples

5.3.2 AISI 430 Ferritic Stainless Steel

Pole figures of {1,1,0} obtained from the EBSD analyses for ferritic samples are shown in Figure 5.3.10. It can be seen in Figure 5.3.10(a) that there are some preferential alignments of {1,1,0} on some directions in the 9 mm base sample, due to the production process of the material. Figure 5.3.10(b) and Figure 5.3.10(c) shows the pole figures of 7 mm and 6.5 mm samples, respectively. In both figures alignment of {1,1,0} perpendicular to the RD and the formation of a fiber texture caused by wire drawing can be seen.

Figure 5.3.10(d) and Figure 5.3.10(e) shows the pole figures of the {1,1,0} for the tensile tested specimen, away from neck and necking area, respectively. Evolution of the fiber texture and the alignment of the {1,1,0} perpendicular to the RD are also confirmed by pole figures of the tensile tested samples. There is a strong alignment of the {1,1,0} perpendicular to the RD in the pole figure obtained from the neck area of the tensile tested sample but this alignment is observed weaker away from the neck. The difference between the pole figures of wiredrawn and tensile tested samples due to the additional forces acting on the material during the drawing process as explained in Chapter 5.3.1.

(a)   (b)

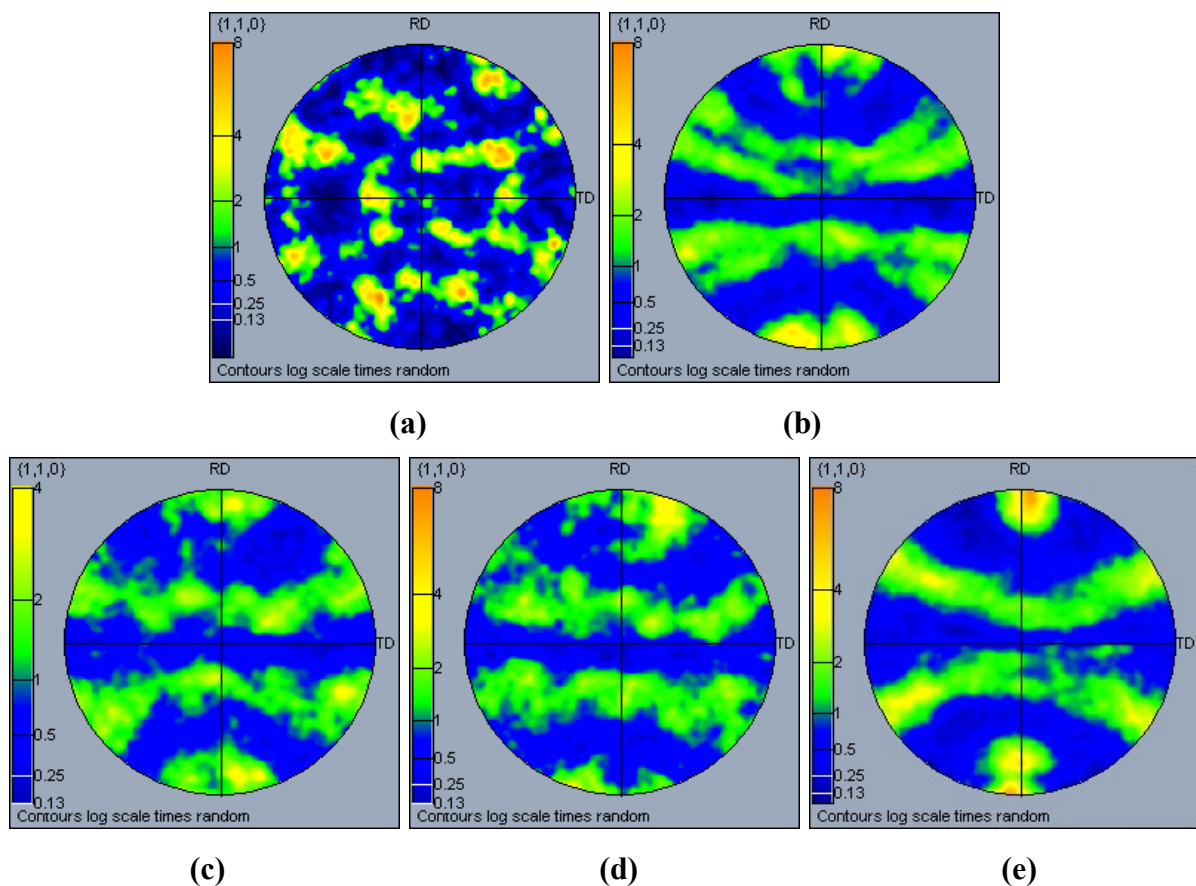(c)   (d)   (e)

Figure 5.3.10 Pole figures of {1,1,0} obtained from EBSD analyses for AISI 430 (a) 9 mm (b) 7 mm (c) 6.5 mm (d) tensile tested (away from neck) (e) tensile tested (necking area) sample

Inverse pole figures of RD obtained from EBSD analyses for ferritic samples are shown in Figure 5.3.11. It can be seen from Figure 5.3.11(a) that there is a strong alignment of [311] parallel to the RD in the 9 mm base sample. For the 7 mm sample, there are alignments of [101] and [302] parallel to the RD as seen in Figure 5.3.11(b). 7 mm sample is behaving like a threshold and with the increasing deformation alignment of [302] parallel to RD tends to dominate the alignment of [101] and the material tends to align only [302] to the RD in the 6.5 mm sample as seen in Figure 5.3.11(c). There is also some activation of [311] in the 6.5 mm sample which can be the result of a possible breakdown of the grains into sub-grains. Those sub-grains are showing a texture landscape similar to a recrystallized texture.

Figure 5.3.11(d) and Figure 5.3.11(e) are the IPF's of the tensile tested samples in which different behaviors can be observed away from the neck and the necking area. Away from the neck, alignment of [302] parallel to RD is observed as in the wiredrawn samples. However, in the necking area, due to the very high amount of deformation, alignment of [101] parallel to RD is observed.

(a)   **(b)**

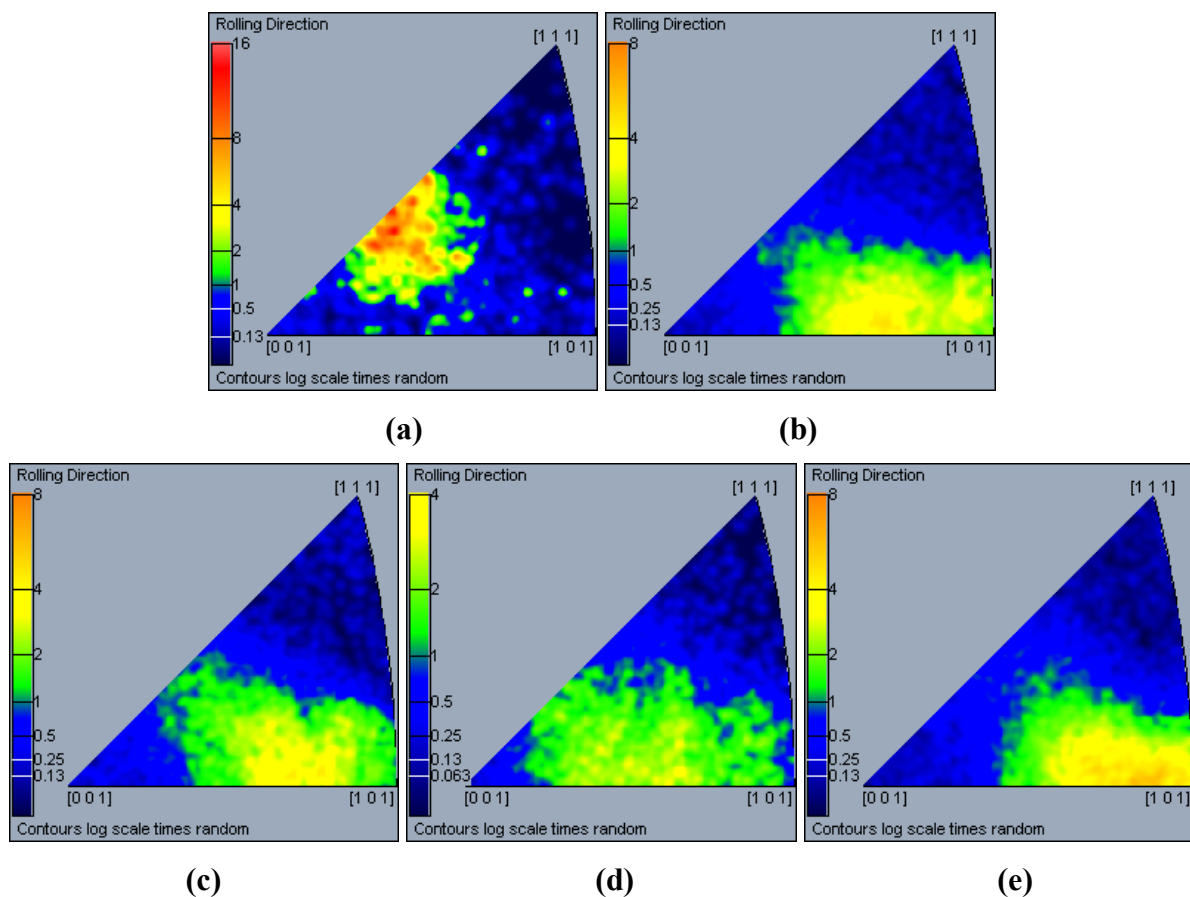**(c)**   **(d)**   **(e)**

Figure 5.3.11 Inverse polar figures parallel to rolling direction for AISI 430 (a) 9 mm (b) 7 mm (c) 6.5 mm and (d) tensile tested (away from neck) (e) tensile tested sample (necking area) sample obtained from EBSD analyses

Figure 5.3.12, Figure 5.3.13 and Figure 5.3.14 show the ODF plots obtained from EBSD analyses for the AISI 430 ferritic stainless steel 9 mm, 7 mm and 6.5 mm samples, respectively. ODF plots of the tensile tested sample away from neck can be seen in Figure 5.3.15 and necking area in Figure 5.3.16.

An intense α-fiber from Goss to Brass textures is observed in all the ODF plots. With the increasing deformation intensity of α-fiber also increases. There is also a strong S texture and intensification of β-fiber.
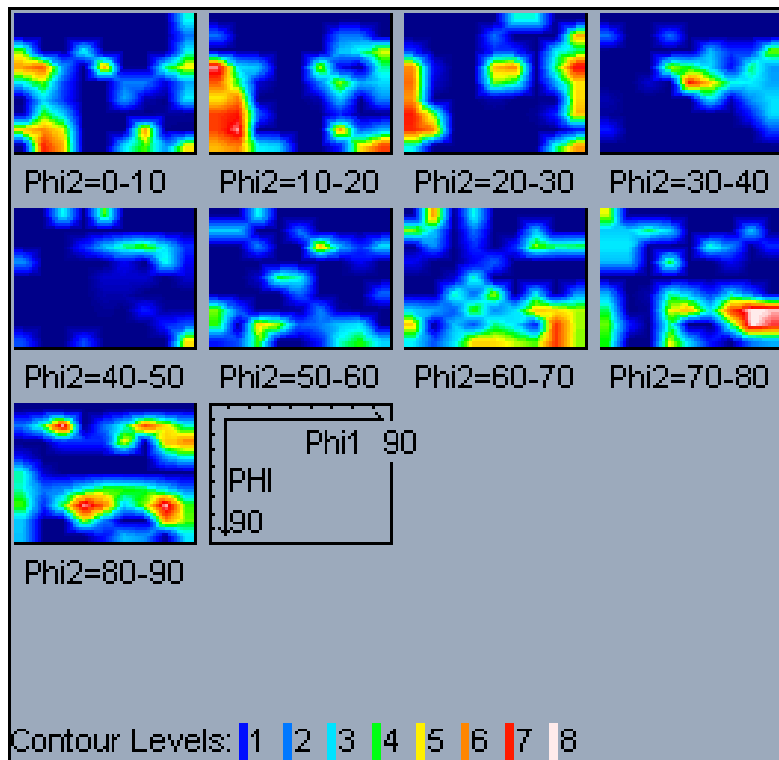

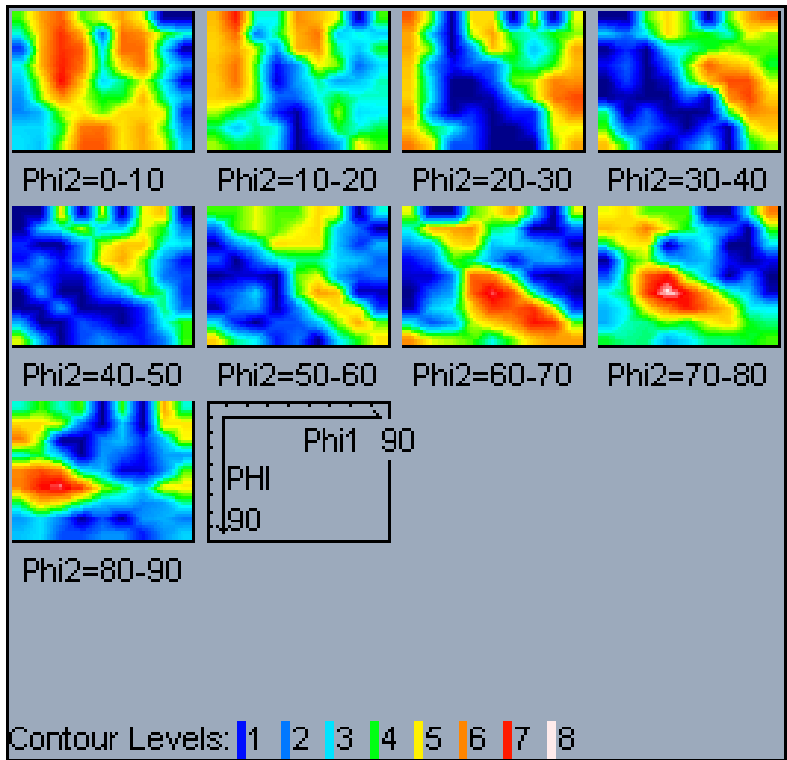**Figure 5.3.12 ODF plots for AISI 430 9 mm sample with changing φ_2 Euler angles**

Figure 5.3.13 ODF plots for AISI 430 7 mm sample with changing φ_2 Euler angles
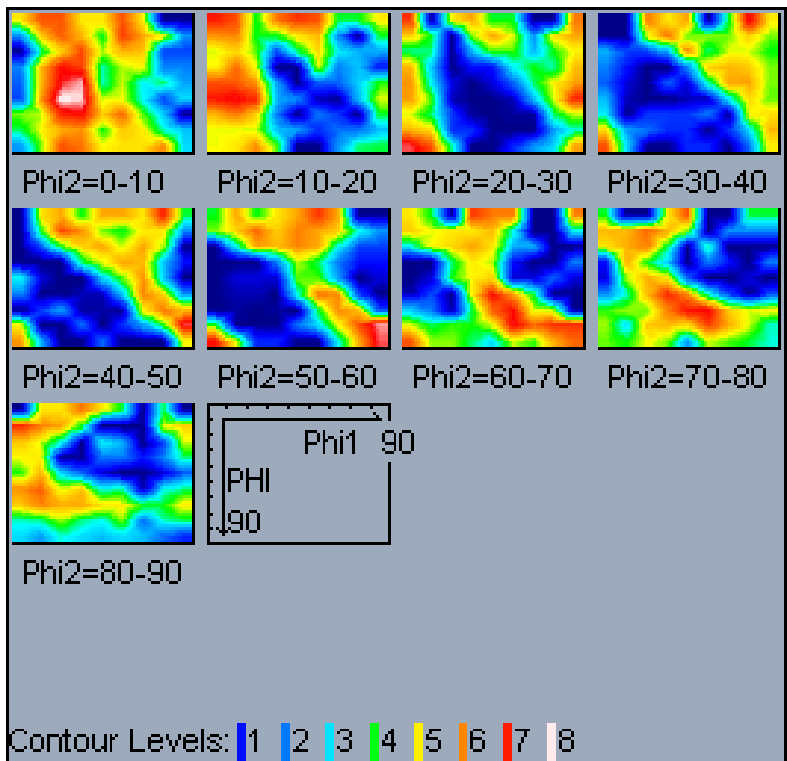

Figure 5.3.14 ODF plots for AISI 430 6.5 mm sample with changing φ_2 Euler angles
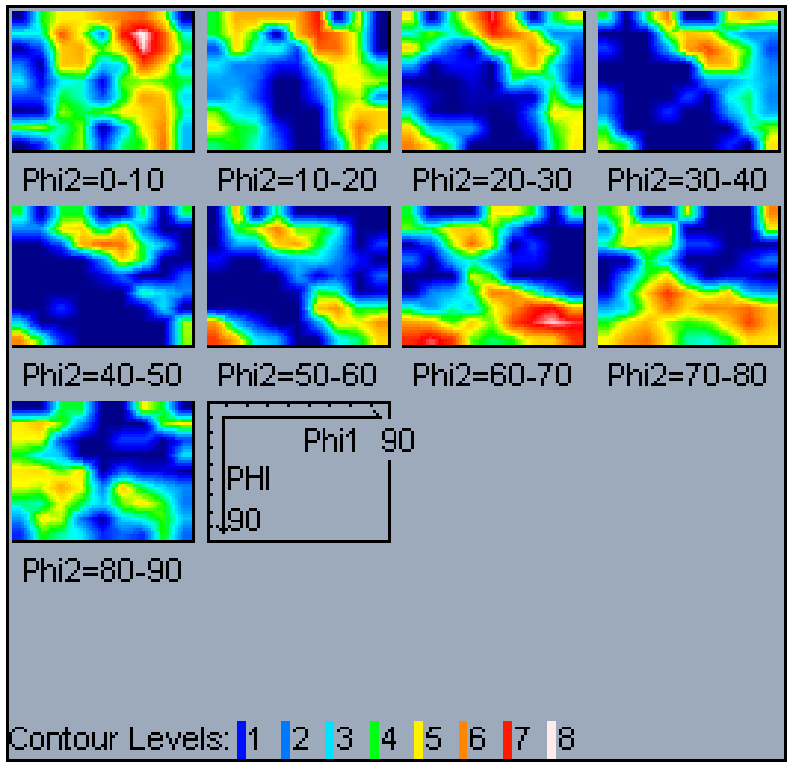
Figure 5.3.15 ODF plots for AISI 430 tensile tested sample (away from neck) with changing φ_2 Euler angles
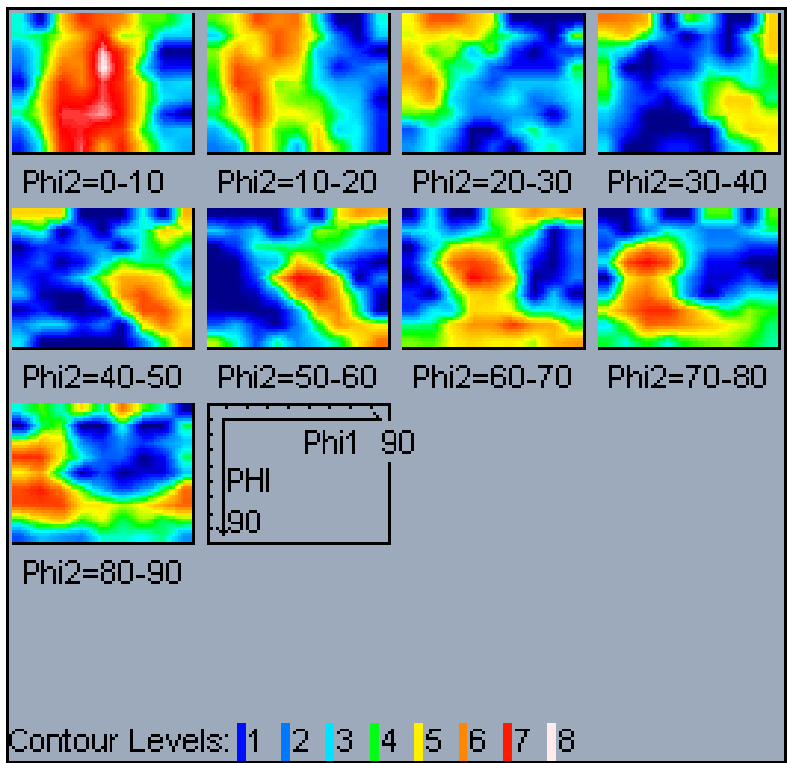

Figure 5.3.16 ODF plots for AISI 430 tensile tested sample (from necking area) with changing φ_2 Euler angles

Figure 5.3.17 shows the CSL graphs of ferritic stainless steel samples. The situation for the ferritic samples is quite complicated because not only the Σ3 special boundaries are evident but also the Σ13 special boundaries are present. Σ3 is always related to twinning while Σ13 is related to recrystallization of ferritic grains. Increasing the deformation, it is observed that both the CSL number of the Σ3 and Σ13 decrease. This behavior is consistent with the decreasing tendency of the experimental values of the strain hardening exponents.
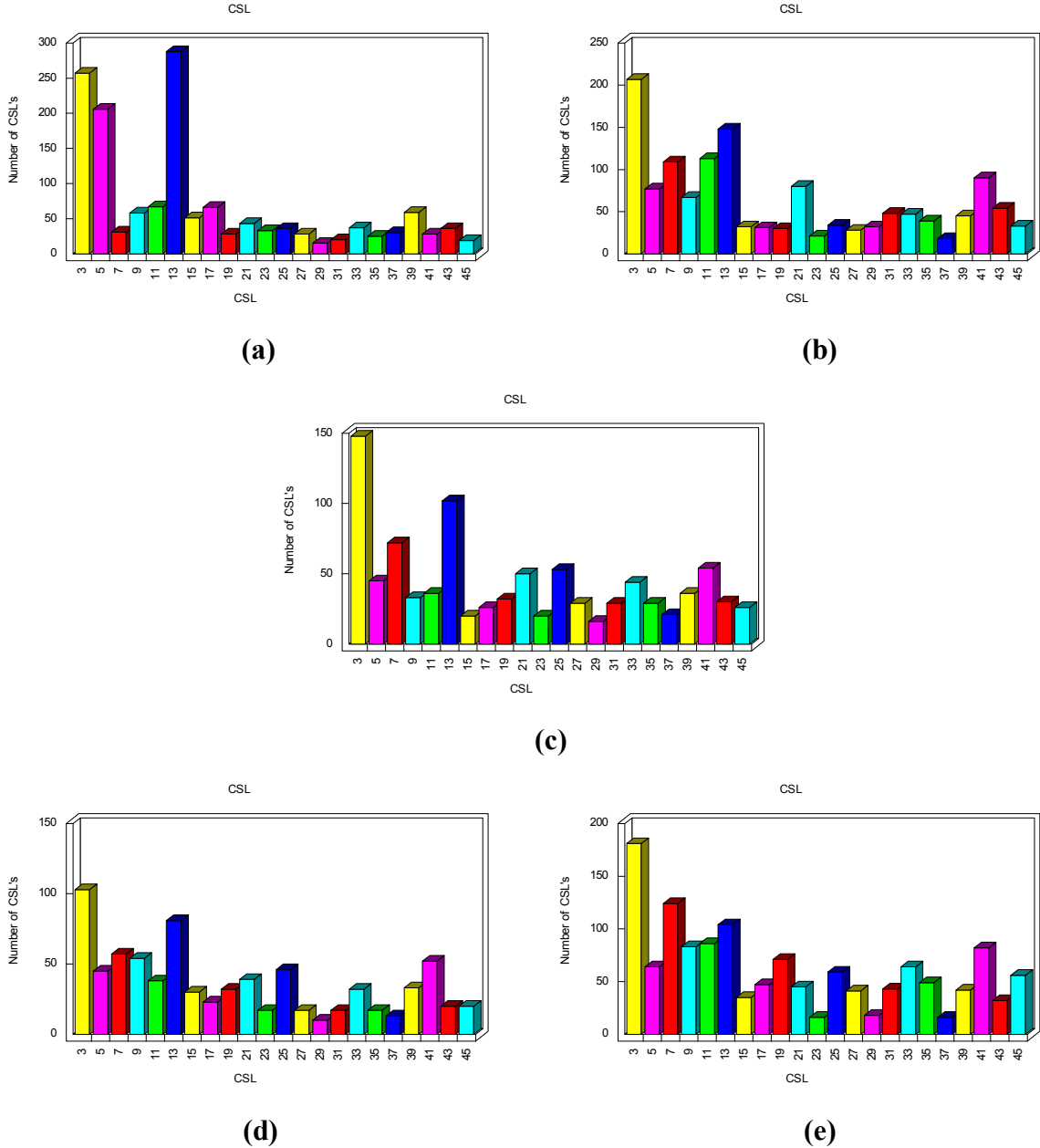

(a)

(b)

(c)

(d)

(e)

Figure 5.3.17 CSL graphs for the AISI 430 (a) 9 mm (b) 7 mm (c) 6.5 mm (d) tensile tested (away from neck) (e) tensile tested (necking area) samples

Distributions of misorientation angles of boundaries for the ferritic samples are shown in Figure 5.3.18. It is observed that in the 9 mm base sample misorientations are mostly at low angles (<5°). By increasing the deformation, the misorientations tend to disperse through higher angles but still the misorientation angles are low. Increase in the deformation causes an increase of dispersion of the angle of misorientations. Thus, this behavior is related to the decreasing trend of the experimental values of the strain hardening exponents.
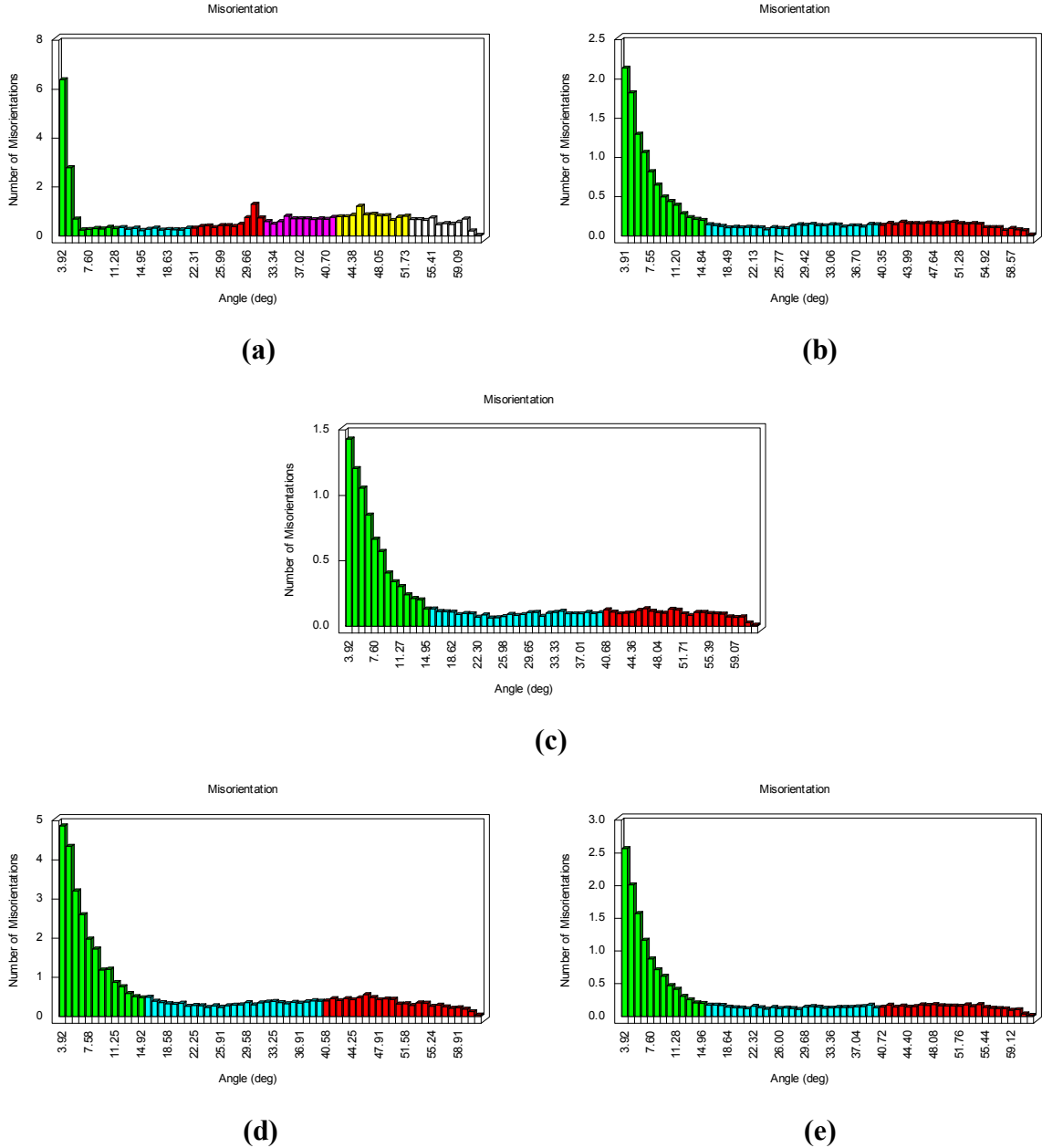

(a)

(b)

(c)

(d)

(e)

**Figure 5.3.18 Misorientation graphs for the AISI 430 (a) 9 mm (b) 7 mm (c) 6.5 mm
(d) tensile tested (away from neck) (e) tensile tested (necking area) samples**

6 Conclusion

In this study, strain hardening phenomenon of wiredrawn AISI 316L austenitic stainless steels and AISI 430 ferritic stainless steels was aimed to be understood. Samples were examined under optical microscope for microstructural characteristics, proper tensile tests were conducted to obtain mechanical properties and finally EBSD analyses were done to acquire information about the textures formed during both wire drawing and tensile testing. The results of the study can be summarized as:

Mechanical properties:

- As the amount of deformation applied to the wires by drawing process increases, the mechanical properties such as; yield strength and ultimate tensile strength increase for both AISI 316L and AISI 430.

Strain-hardening exponent:

- For AISI 316L, relatively high value of strain-hardening exponent (*n*) of 9 mm base sample shows a dramatic decrease in the first step of drawing but further drawing results in an increasing trend of the exponent.
- For AISI 430, by the increasing deformation up to the diameter of 7 mm, a decreasing trend for strain-hardening exponent is observed. Further drawing to 6.5 mm diameter results in an increase of the strain hardening exponent caused by possible breakdown of the grains into sub-grains.

Texture evolution:

- EBSD results show that, Goss, Brass, Cube and Rotated Cube textures are present in the 9 mm base sample of AISI 316L. By the increase of deformation, intensification of RC{001}<101> and B{011}<112> textures, and formation of S{123}<634> are observed. During drawing from 7 mm to 6.5 mm the α-fiber tends to disappear and transform into a strong β-fiber.
- An intense α-fiber is observed in all the samples of AISI 430. By the increase of deformation the intensity of α-fiber also increases. There is also a strong S texture and intensification of β-fiber.

In conclusion, the strain hardening appears to be strictly related to crystallographic texture evolution induced by the applied cold drawing process.

References

[1] M. Zidani, S. Messaoudi, T. Baudin, D. Solas and M. H. Mathon, "Deformation Textures in Wire Drawn Perlitic Steel," *Int J Mater Form,* vol. 3, pp. 7-11, 2010.

[2] "Strengthening/Hardening Mechanisms," NDT Resource Center, [Online]. Available: http://www.ndt-ed.org/EducationResources/CommunityCollege/Materials/Structure/strengthening.htm. [Accessed 07 2012].

[3] R. W. Davidge, Mechanical Behaviour of Ceramics, Cambridge Solid State Science Series, Syndics of the Cambridge University Press, 1979.

[4] J. Zarzycki, Glasses and Vitrious State, Cambridge Solid State Science Series, Press Syndicate of the University of Cambrigde, 1991.

[5] W. D. Callister Jr., Materials Science and Engineering: An Introduction - 7th Ed., New York: John Wiley & Sons, Inc., 2007.

[6] J. T. Black and R. A. Kohser, DeGarmo's Materials and Processes in Manufacturing 10th Ed., John Wiley and Sons Inc., 2008.

[7] D. R. Askeland, P. P. Fulay and W. J. Wright, The Science and Engineering of Materials 6th Ed., CL Engineering, 2010.

[8] J. Beddoes and M. J. Bibby, Principles of Metal Manufacturing Processes, Elsevier Butterworth-Heinemann, 2003.

[9] G. E. Dieter, Mechanical Metallurgy, McGraw-Hill Book Co, 1988.

[10] R. N. Wright, Wire Technology: Process Engineering and Metallurgy, Elsevier Inc., 2011.

[11] A. El-Domiaty and S. Z. Kassab, "Temperature Rise in Wire-Drawing," *Journal of Materials Processing Technology,* vol. 83, pp. 72-83, 1998.

[12] *ISO 6892-1: Metallic materials - Tensile testing - Part 1: Method of test at room temperature,* International Organization for Standardization, 2009.

[13] T. Maitland and S. Sitzman, "Electron Backscatter Diffraction (EBSD) Technique and Materials Characterization Examples," in *Scanning Microscopy for Nanotechnology Techniques and Applications*, Springer, 2007, pp. 41-75.

[14] O. C. Wells, "Comparison of Different Models for the Generation of Electron Backscattering Patterns in the Scanning Electron Microscope," *Scaning,* vol. 21, no. 6, pp. 368-371, 1999.

[15] M. Hatherly ve W. B. Hutchinson, An Introduction to Textures in Metals, Institution of Metallurgists, 1979.

[16] H. R. Wenk and P. Van Houtte, "Texture and Anisotropy," *Reports on Progress in Physics,* vol. 67, pp. 1367-1428, 2004.

[17] O. Engler and V. Randle, Introduction to Texture Analysis: Macrotexture, Microtexture, and Orientation Mapping 2nd Ed., CRC Press, 2010.

[18] "What is the inverse pole figure?," Resmat, [Online]. Available: http://www.resmat.com/resources/chapter7.htm. [Accessed 04 07 2012].

[19] F. J. Humphreys and M. Hatherly, Recrystallization and Related Annealing Phenomena, 2nd Edition, Elsevier Ltd., 2004.

[20] *Product Data Sheet 316/316L Stainless Steel,* AK Steel Corporation, 2007.

[21] *ASM Metal Handbook, Vol. 1, Properties and Selection: Irons, Steels, and High Performance Alloys,* ASM International, 2005.

[22] *Product Data Sheet 430 Ferritic Stainless Steel,* AK Steel Corporation, 2007.

[23] *ASM Metal Handbook, Vol. 9, Metallography and Microstructures,* ASM International, 2004.

[24] M. Godec, "Material Failure of an AISI 316L Stainless Steel Hip Prosthesis," *Materials*

and Technology, vol. 45, no. 2, pp. 85-90, 2011.